Conf-820356--8

UCRL-86956
PREPRINT

UCRL--86956

DE82 015167

REVIEW OF UPCONVERTED ND-GLASS LASER PLASMA EXPERIMENTS AT THE LAWRENCE LIVERMORE NATIONAL LABORATORY

K. R. Manes

This paper was prepared for submittal to
Ultraviolet Spectroscopy Meeting
Boulder, Colorado
March 8-10, 1982

May 1982

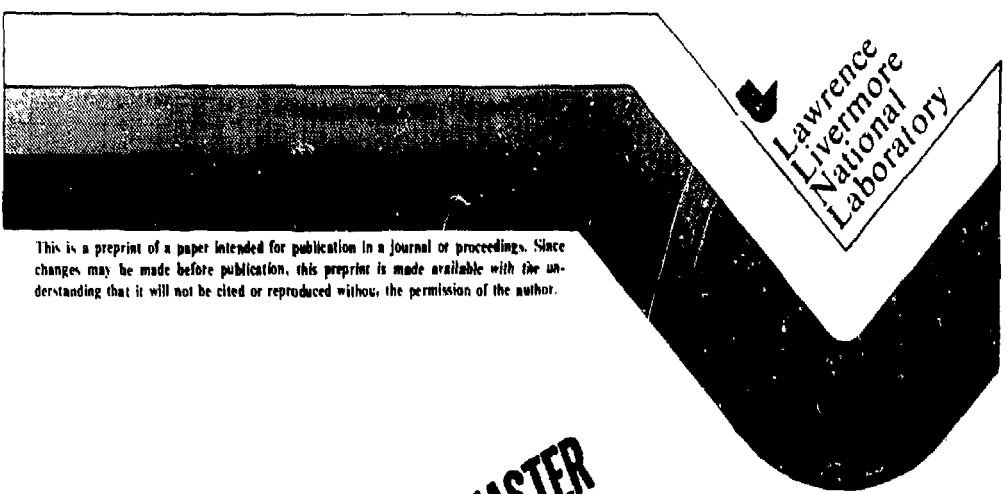

REVIEW OF UPCONVERTED ND-GLASS LASER PLASMA EXPERIMENTS AT THE LAWRENCE LIVERMORE NATIONAL LABORATORY*

K. R. Manes
Lawrence Livermore National Laboratory
Livermore, California 94550

INTRODUCTION

Systematic scaling experiments aimed at deducing the dependence of laser-plasma interaction phenomena on target plasma material and target irradiation history have been underway in laboratories all over the world in recent years.[1-5] During 1980 and 1981 the Livermore program undertook to measure the laser light absorption of high and low Z plasmas and the partition of the absorbed energy amongst the thermal and suprathermal electron populations as a function of both laser intensity and wavelength.[3-5] Simulations suggested that short wavelength laser light would couple more efficiently than longer wavelengths to target plasmas.[6,7] Shorter wavelength heating of higher electron plasma densities would, it was felt, lead to laser-plasma interactions freer of "annomalous" absorption processes.[8,9] The following sections review LLNL experiments designed to test these hypotheses.

ABSORPTION STUDIES

The experiments discussed here were carried out using the Argus and Shiva lasers.[10,11] Figure 1 shows the Argus target area where upconverted laser light was typically directed onto 600 μm diameter (Au, Be, Ni, Ti, CH) disk targets by f/2.2 lenses.[3] Many of the instruments mounted on the target chamber are x-ray spectrometers. The first step in measuring the disposition of laser energy is to determine the optical absorption of the target plasma. Absorption, in this context, is taken to mean the fraction of the incident laser energy not accounted for by reflected beam diagnostics. A schematic diagram of the Argus experiments, Figure 2, shows one of the 28 cm diameter Argus 1.06 μm laser beams down collimated to 10 cm, frequency doubled and tripled by KDP crystals and focused onto a target located within an enclosing "box calorimeter."

Target irradiation conditions for absorption studies and the x-ray measurements which followed are summarized in Table I. Laser intensities noted are spatial average values at the peak of the temporal pulse. Although the near field Argus laser beam presented to the focusing lens was very uniform (typically less than 10% intensity modulation on the beam), passive phase errors from the many optical components accumulated to produce highly structured beam profiles at the targets.

* Work performed under the auspices of the U. S. Department of Energy by the Lawrence Livermore National Laboratory under Contract No. W-7405-ENG-48.

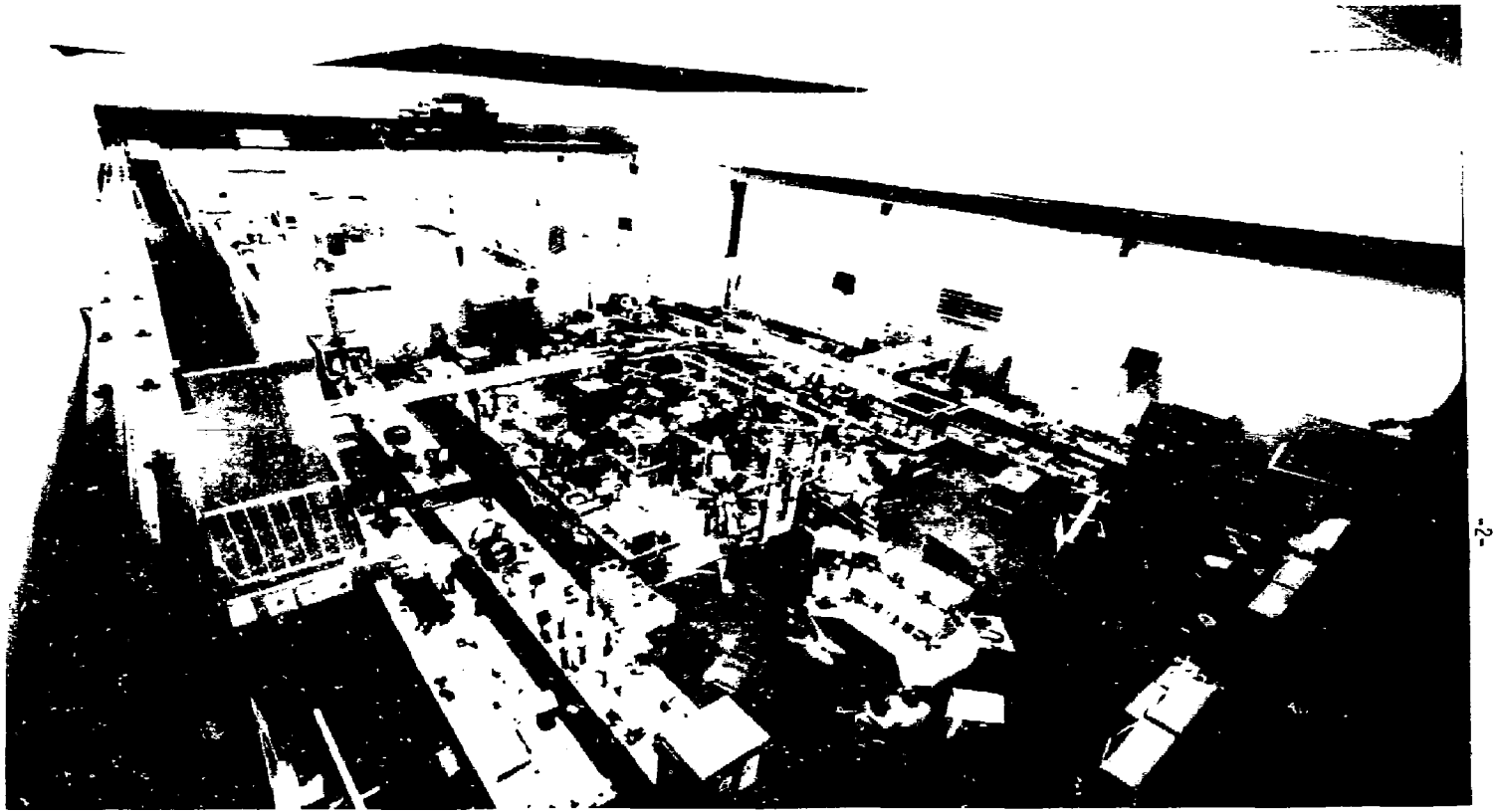

Fig. 1 Argus laser facility with the target area in the foreground. The target chamber with its optical and x-ray diagnostic instruments is located in the center of the room.

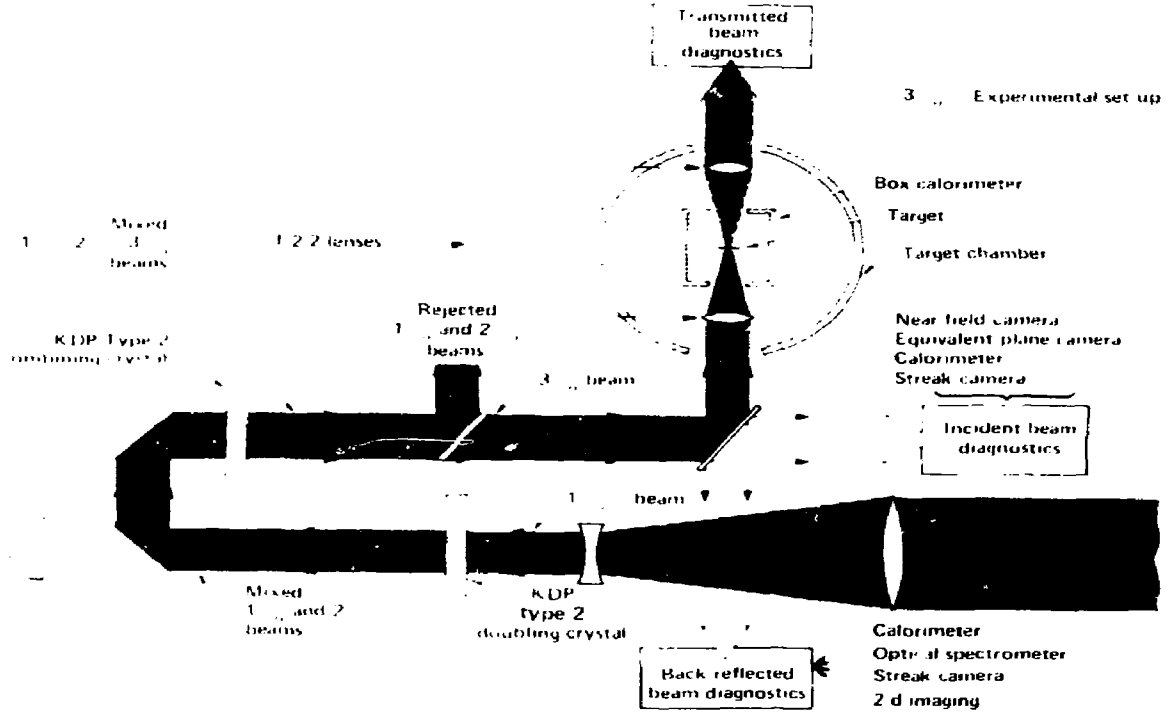

Fig. 2 Experimental layout for wavelength scaling experiments in the Argus facility.

TABLE I Irradiation Conditions at $1\omega_0$, $2\omega_0$ and $3\omega_0$

- **Incident laser energy:**

  $3\omega_o$ $\quad 4J \leqslant E_{inc} \leqslant 40J$

  $2\omega_o$ $\quad 4J \leqslant E_{inc} \leqslant 200J$

  $1\omega_o$ $\quad 4J \leqslant E_{inc} \leqslant 10kJ$

  - Minimum energy: diagnostics limited
  - Maximum energy: damage limited

- **Laser pulse duration: 600 to 700 ps FWHM**

- **Focus:**

  Argus: f/2.2, P polarization

  Shiva: 20 f/6 beams, radial polarization

- **Spot diameters:**

  $\sim 150\ \mu m$ for $I \sim 3 \times 10^{13}$ W/cm^2

  $\sim 150\ \mu m$ and $\sim 100\ \mu m$ for $I \sim 3 \times 10^{14}$ W/cm^2

  $\sim 100\ \mu m$ and less for $I \gtrsim 10^{15}$ W/cm^2

Figure 3 quantifies this situation with intensity distribution functions measured on typical shots at each wavelength. Beam quality degraded with upconversion so that the $3\omega_0$ beams contained the most fine structure and showed very strong modulation. It should be noted here that each optical element employed met or exceeded the $\lambda/4$ optical flatness criterion before it was used in the laser system. Because of their large output apertures, future large Nd-glass lasers, such as Nova, will probably use arrays of conveniently sized nonlinear crystals in order to upconvert their pulses. Still more distorted target plane intensity distributions can be expected in these devices due to slightly mismatched crystals and diffraction from crystal interstices. Designers of directly illuminated capsules will encounter great difficulty in meeting their beam uniformity requirements. In the following, "intensities" will always refer to spatial mean intensity and error bars will denote plus or minus one standard deviation about this mean value.

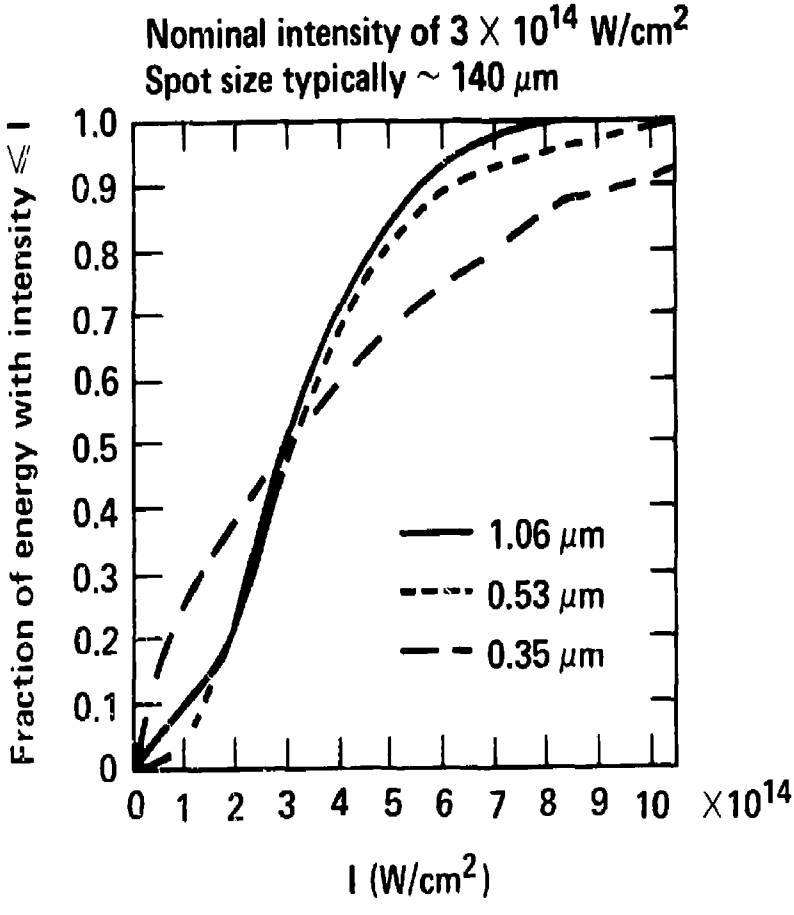

Fig. 3 Target plane intensity distribution function at 1 μm, 0.5 μm and 0.35 μm.

Enclosing or "box calorimeters" have often been used at LLNL.[22] Unabsorbed laser light passes through transparent ion shields (Schott WG-280) indicated in Figure 4 and is absorbed in the walls of the calorimeter. Each laser wavelength imposes a different set of criteria on the calorimeter components. For example, the infrared fundamental and the second harmonic green light can be absorbed on calorimeter walls clad with Schott NG-1 while ultraviolet third harmonic radiation was measured using Schott GG-19 absorber. At intervals the WG-280 ion shields which intercept target debris were replaced. On several occasions during the experiments quartz shields were substituted, but no difference in box calorimeter performance was noted. The calorimeter was recalibrated

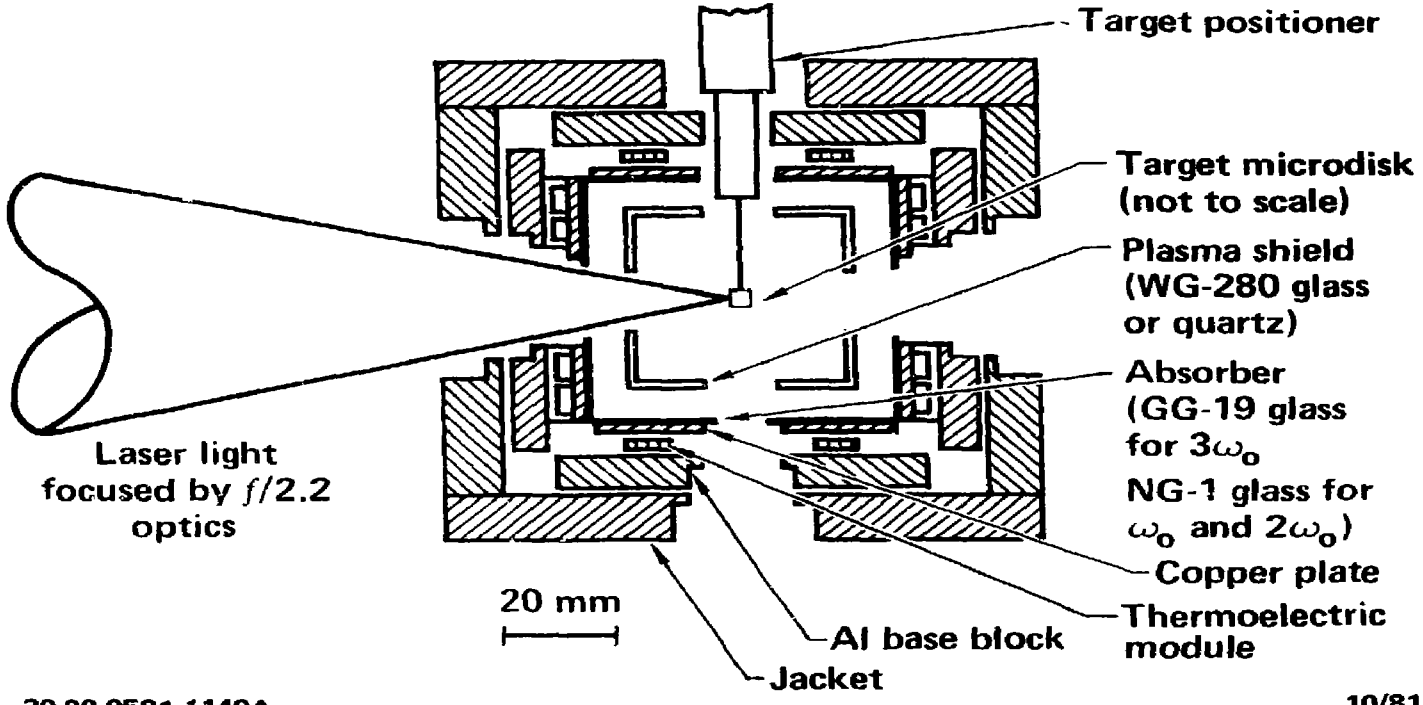

Fig. 4 Target irradiation was done inside a box calorimeter to measure scattered laser light.

before and after each experiment and its integrity checked during the shot sequence.

Figure 5a groups absorption measurements made on Au plasmas according to incident laser wavelength while Figure 5b shows similar measurements carried out on low Z Be plasmas. The general trends characteristic of classical collisional absorption, inverse bremsstrahlung, are apparent in these data. At a given intensity, shorter wavelength light was absorbed more efficiently by higher Z plasmas. The scattering of incident third harmonic light by the plasmas was often too low to register above background in the calorimeter.

In preparation for x-ray conversion efficiency measurements and to check for any residual resonance absorption contribution, absorption versus target tilt for p-polarized irradiation was measured.[22] As expected, the f/2.7 focusing system introduced a wide enough range of incident ray angles so that the 600 to 700 ps Gaussian laser pulses were absorbed with only a weak dependence on the angle between the beam axis and the target normal. Figure 6 shows that no detectable difference in absorption was noted for tilts as large as plus or minus 30° from the converging laser beam axis. This leads to the conclusion that resonance absorption plays a relatively minor role in these measurements.

Laser light scattered from the target into the focusing lens cone was analysed by time resolved backscatter spectrometers. A decided red shift characteristic of scattering from laser driven ion waves, stimulated Brillouin scattering, can be seen in all of this data; typical examples of which are reproduced in Figure 7c.[5] If the observed spectral shifts are viewed as the result of competition between stimulated Brillouin scattering and the Doppler shift imposed by an expanding plasma, the measured backscattered spectra as the targets are tilted provide a crude estimate of coronal electron temperature.[12] Figure 7a and b are reproduced from Rosen et al (Ref. 12) wherein it is observed that the Brillouin red shift, f_B, should be reduced by the Doppler blue shift, f_D, of outward moving matter. Since that matter blows off roughly normal to the face of the disk, tilted disk spectra should show a smaller Doppler blue shift. In making an estimate of matter velocity from spectral shifts and in the soft x-ray conversion measurements which will be described next, the assumption is implicit that laser heated plasmas of like material which absorb like amounts of energy of a given wavelength, intensity and pulse duration are essentially identical even though they are irradiated at different incidence angles. With this in mind, the observed average spectral shifts may be written

$$\Delta f(\theta) \cong f_B + f_D \cos\theta \qquad (1)$$

Where θ is the angle between the target normal and the laser beam/observation axis. Table II summarizes the velocities inferred from the spectra in Figure 7 using Lasnex estimates for the average ionic charge state, $\bar{Z}$, at $N_e \approx 1/3N_c$.[5,12]

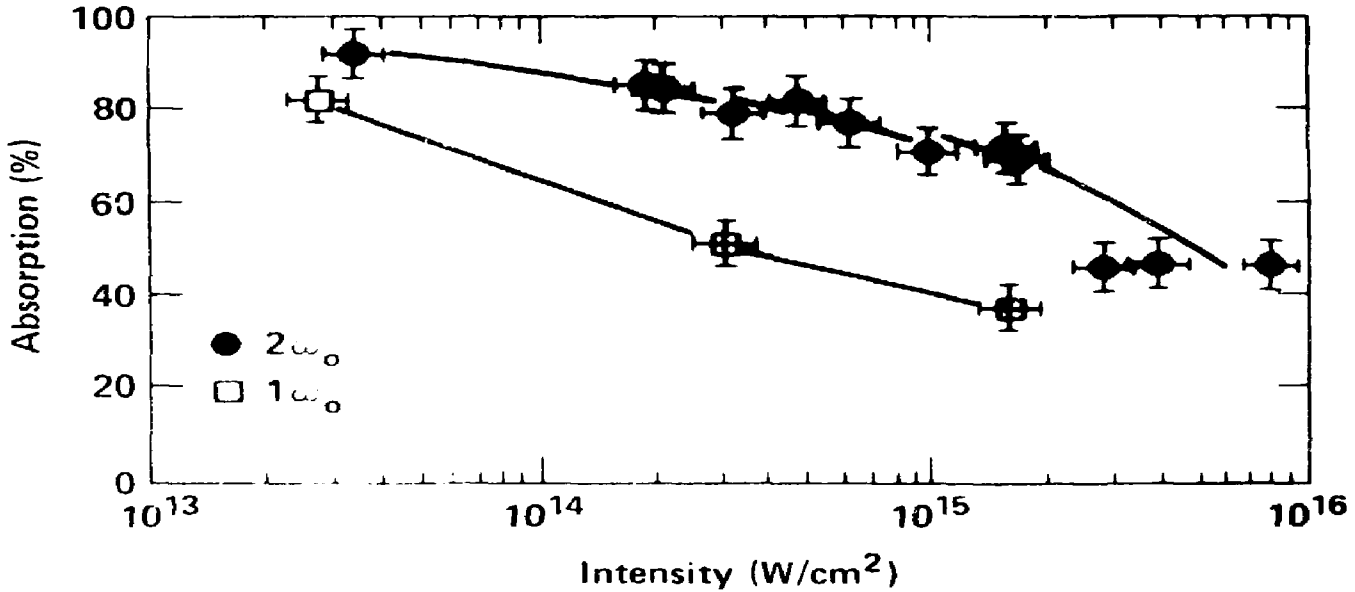

20-90-0381-0677

9/81

Fig. 5a $1\omega_0$, $2\omega_0$ and $3\omega_0$ absorption - Au disk targets.

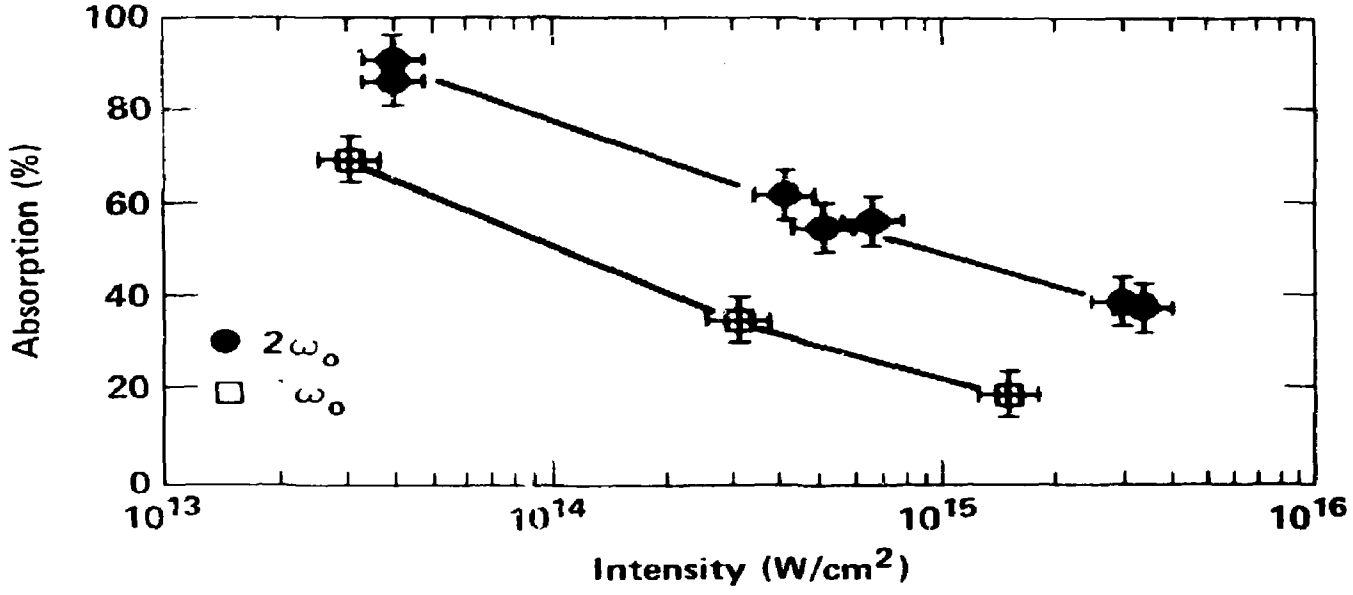

20-90-0381-0676

9/81

Fig. 5b $1\omega_o$, $2\omega_o$ and $3\omega_o$ absorption - Be disk targets.

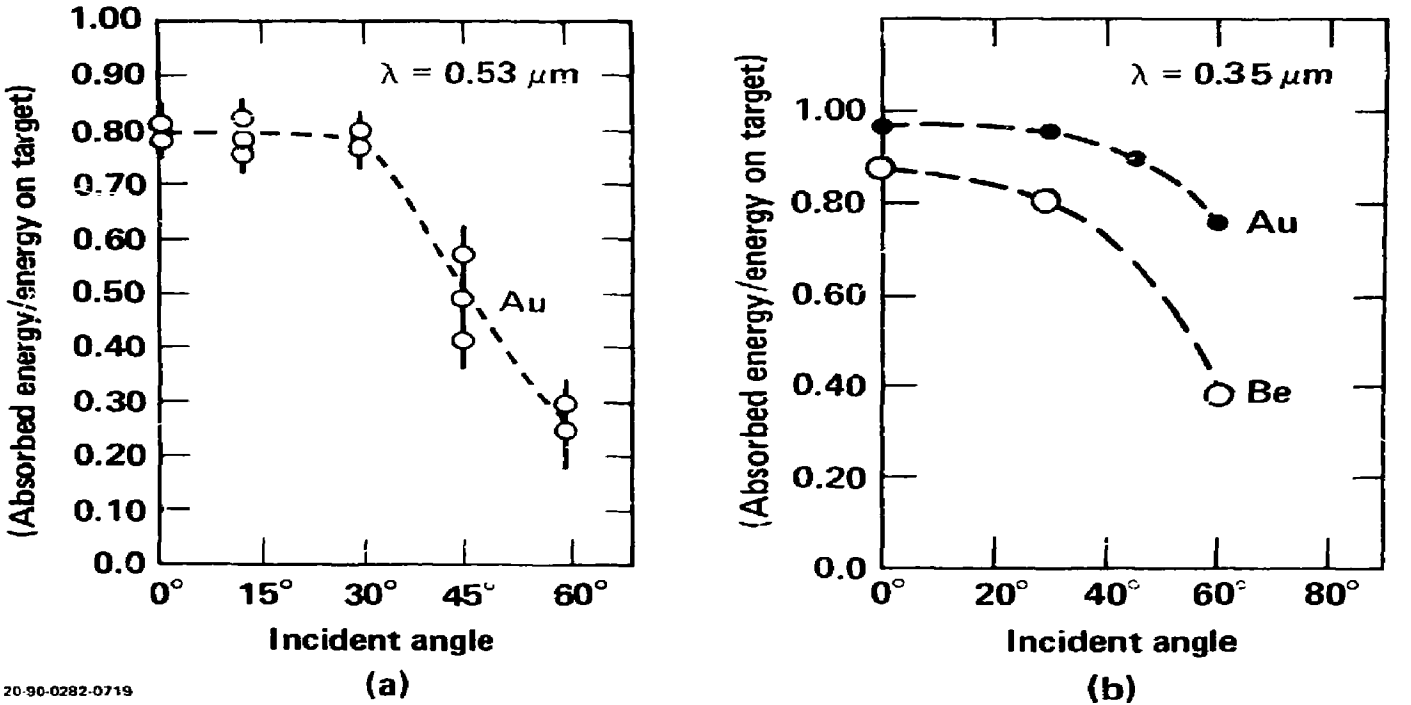

20-90-0282-0719

Fig. 6 The fraction of absorbed energy was investigated for angle of incidence dependence for both high and low Z-targets.

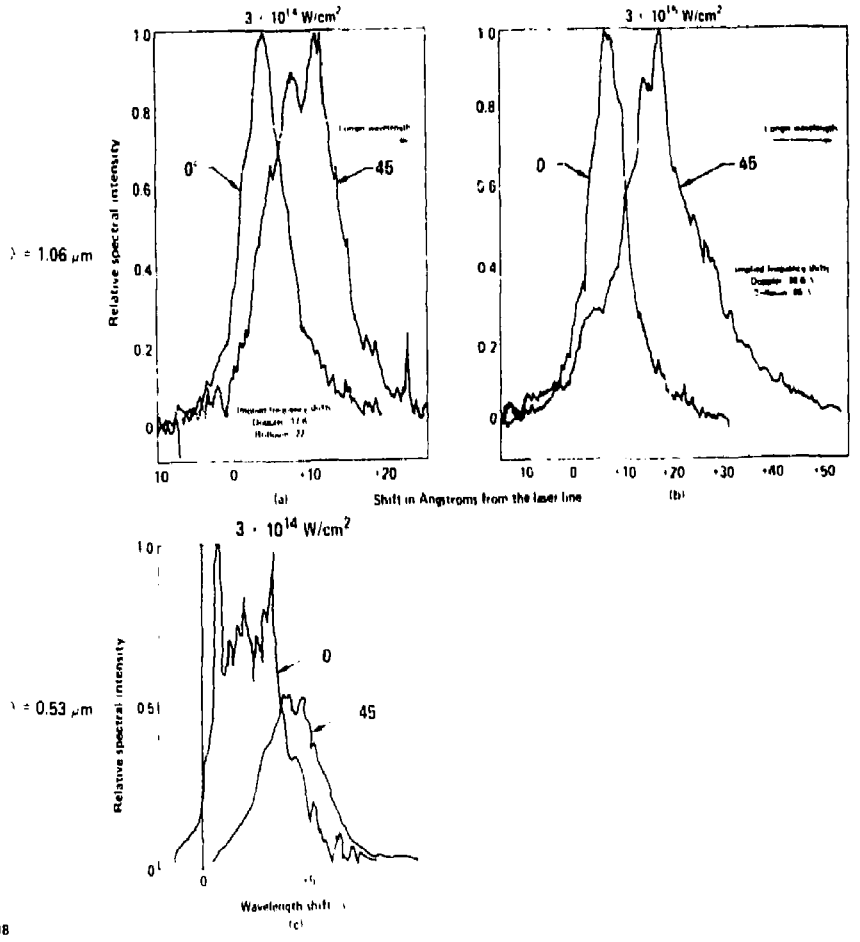

Fig. 7 From the angular dependence of the mean red shift, the Doppler and Brillouin shifts can be separated.

The picture which emerges from simulation calculations is of a progressively more "classical", cooler corona plasma as I or λ is decreased, particularly for high Z targets.[4] Particle-in-cell calculations by Eastabrook et al were carried out in order to arrive at the predictions reproduced in Figure 8.[12,13] While stimulated Brillouin scattering plays a limited role in these calculations, backscattered spectral predictions have thus far failed to account for the large red shifts observed in, for example, Figure 7. The gross features of absorption are satisfactorily modeled now, but the present generation of simulations fails to reproduce reliable low density corona information and is thus limited in predicting optical scattering and

x-ray production adequately.

Table II

Wavelength	Intensity	Z	$\langle T_e \rangle + \frac{3\langle f_1 \rangle}{Z}$	Matter Velocity
1.06 μm	3×10^{14} W/cm^2	51	(5+3) keV	~ 3×10^7 cm/sec
1.06 μm	3×10^{15} W/cm^2	58	(20+10) keV	~ 7×10^7 cm/sec
0.53 μm	3×10^{14} W/cm^2	50	(3.8+1) keV	1.8×10^7 cm/sec

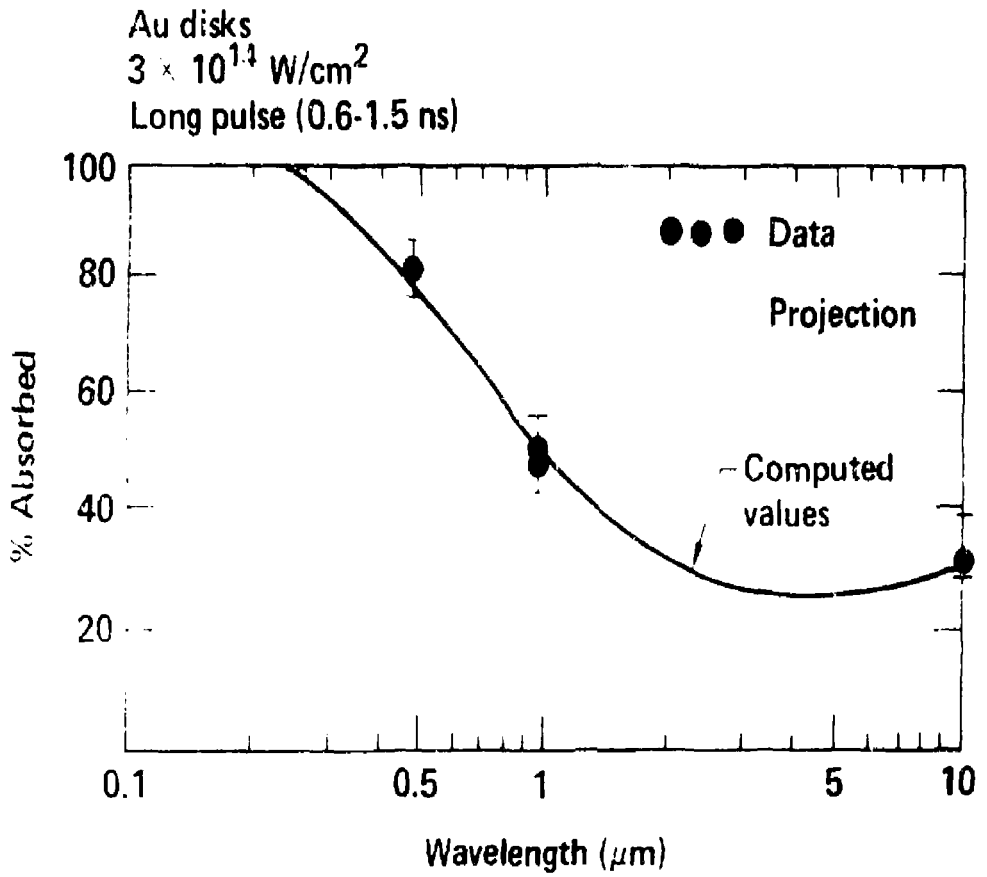

Fig. 8 Predicted wavelength scaling of absorption by high Z materials match experimental results.

SOFT X-RAY CONVERSION STUDIES

[illegible] established, measurements of x-ray conversion efficiency [illegible] laser heated targets, particularly those irradiated for several hundred picoseconds or more, expand in an axially symmetric two dimensional flow which naturally causes the x-ray emitting region to move [illegible].[12,14] Shiva experiments using a streaked x-ray microscope, observed ~10^{14}W/cm^2 irradiations of Au disk targets.[15] Striking photographs such as that in Figure 9 show a thin emission zone moving

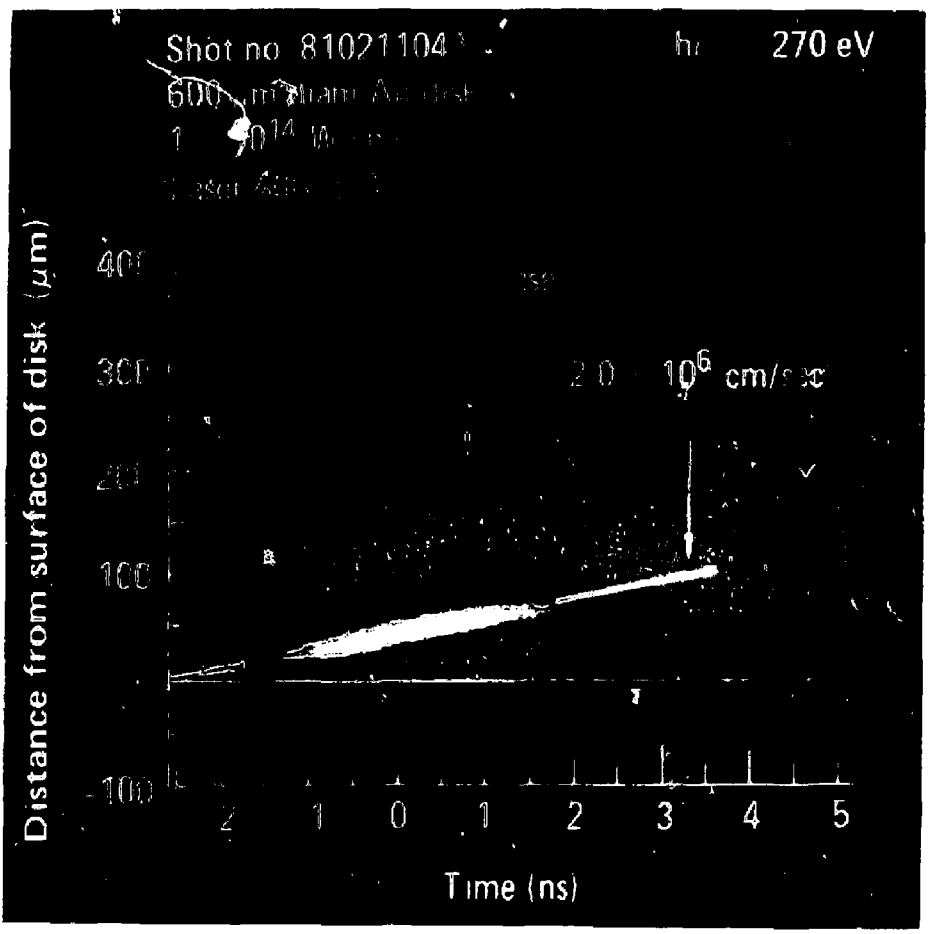

Fig. 9 Streaked x-ray image of a laser irradiated gold disk.

[illegible] away from the target's initial surface at a velocity which scales approximately as the 0.44 power of the peak incident laser intensity. Such observations make it clear that x-ray emitting target surfaces evolve rapidly in time and space. The assumption of either a

spherical or a planar emitting surface can not be safely made and observations at many angles are needed to derive an angular integral of x-ray emission. By the same token, time resolved spectral measurements made over the past several years have consistently reported that laser heated target plasmas are not in local thermodynamic equilibrium.[12] High Z plasmas, such as Au, often emit copious N and M line radiation. Without five or more time resolved channels between approximately 0.1 and 1.5 keV, an accurate x-ray energy accounting is not possible. LLNL x-ray diagnosticians have faced the challenge of performing absolutely calibrated measurements on very bright pulsed sources in hostile environments for over thirty years. The "Dante" instruments used in these studies properly belong to that technology in which spectral resolution is given up for absolute calibration.[5,25] Figure 10 contains a sampling of x-ray spectra recorded in 0.53 μm target irradiations.[4] Clearly, both an angular and a spectral integration must be carried out in order to measure the x-ray conversion efficiency.

At both the Argus and the Shiva target irradiation facilities, ten channel "Dante" x-ray K&L edge filtered x-ray diode systems measured spectra such as those in Figure 10 on each target shot. Three such instruments labled T, L and W and independently absolutely calibrated viewed the targets in the Argus chamber from widely separated angles. As Figure 6 suggests, target tilts in the range of plus or minus thirty degrees have no detectable effect on absorption. It is assumed that soft x-ray emission will be likewise unaffected by target tilts within this range (as no other observable was seen to change). The lines of sight relative to the target normal obtained by +30, +10 and -30 degree tilts, for example, adequately span the important viewing angles as indicated in Figure 11. Note, for example, that Dante L and W share the same polar angle but widely separated azimuthal angles at a target tilt of -30^{o}. This provides a check of the assumed azimuthal symmetry of the x-ray flux.

The angular emission of soft x-ray flux from Au disks heated by 25J, 600 ps, 0.53 μm pulses is displayed in Figure 12. On such a plot, an ideal planar source, a Lambertian emitter, would be represented by a straight line passing through the origin. An ideal spherical source would deliver the same amount of energy into any angle and so would be represented by a horizontal line on Figure 12. The time varying source measured, however, can not be represented by either of these simple shapes without substantial error. Many similar measurement sets provide the conversion efficiency data summarized by Figure 13.[3,4,16] Significantly, the shorter wavelength laser light is converted to soft x-rays with an efficiency of ~60%.

The roll-off in conversion efficiency observed in the 0.53 and 0.35 μm data was not anticipated and is not yet completely understood.[16] Rather, simulations contended that the conversion efficiency should decline monotonically with $I\lambda^2$ at approximately the rate exhibited by the 1.06 μm data.[4]

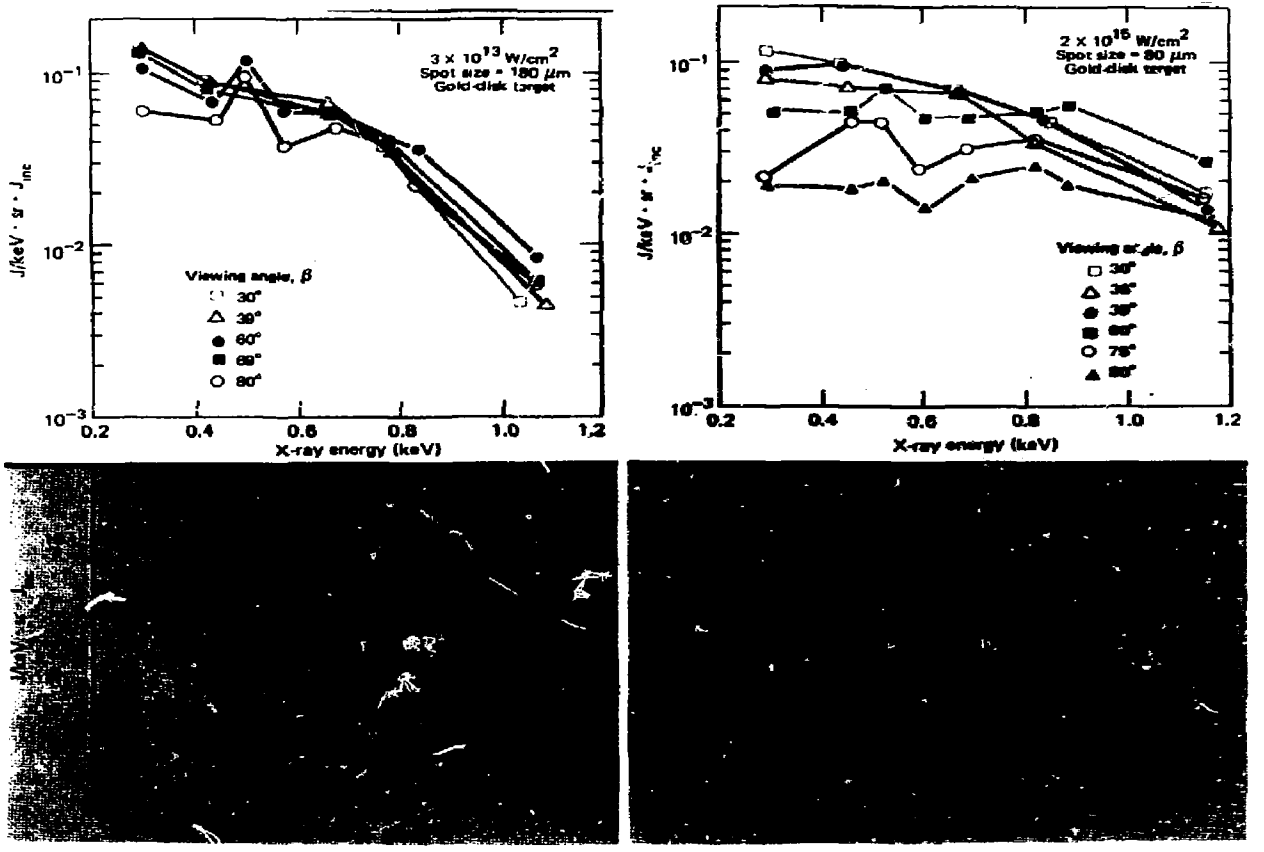

Fig. 10 Typical x-ray spectra from 0.53 μm heated gold disk targets.

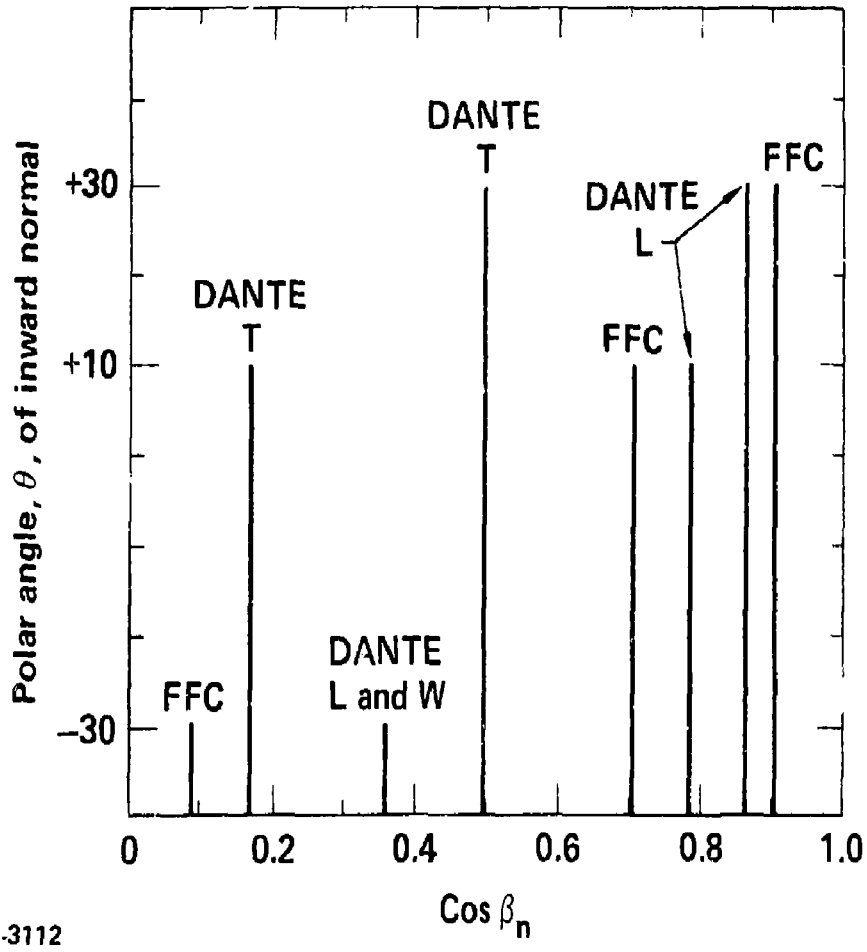

Fig. 11 Soft x-ray diagnostic viewing angles are plotted versus target tilt. Three Dante spectormeters and two broadband "fast flat calorimeter", FFC, were used.[4,5]

The soft x-ray conversion efficiency also varies with target material atomic number, Z. Although angular x-ray distributions were not measured when all of these data were taken, Figure 14 shows that higher Z target plasmas heated with 1.06 μm laser pulses emitted soft x-rays more efficiently than lower Z plasmas.[25,26] Since sub keV x-ray production far from spectral regions dominated by line emission are probably generated by bremsstrahlung of low energy electrons colliding with screened nuclear potentials, it may be more meaningful to plot normalized x-ray energy versus $\bar{Z}$, where $\bar{Z}$ is the LASNEX calculated charge state. As

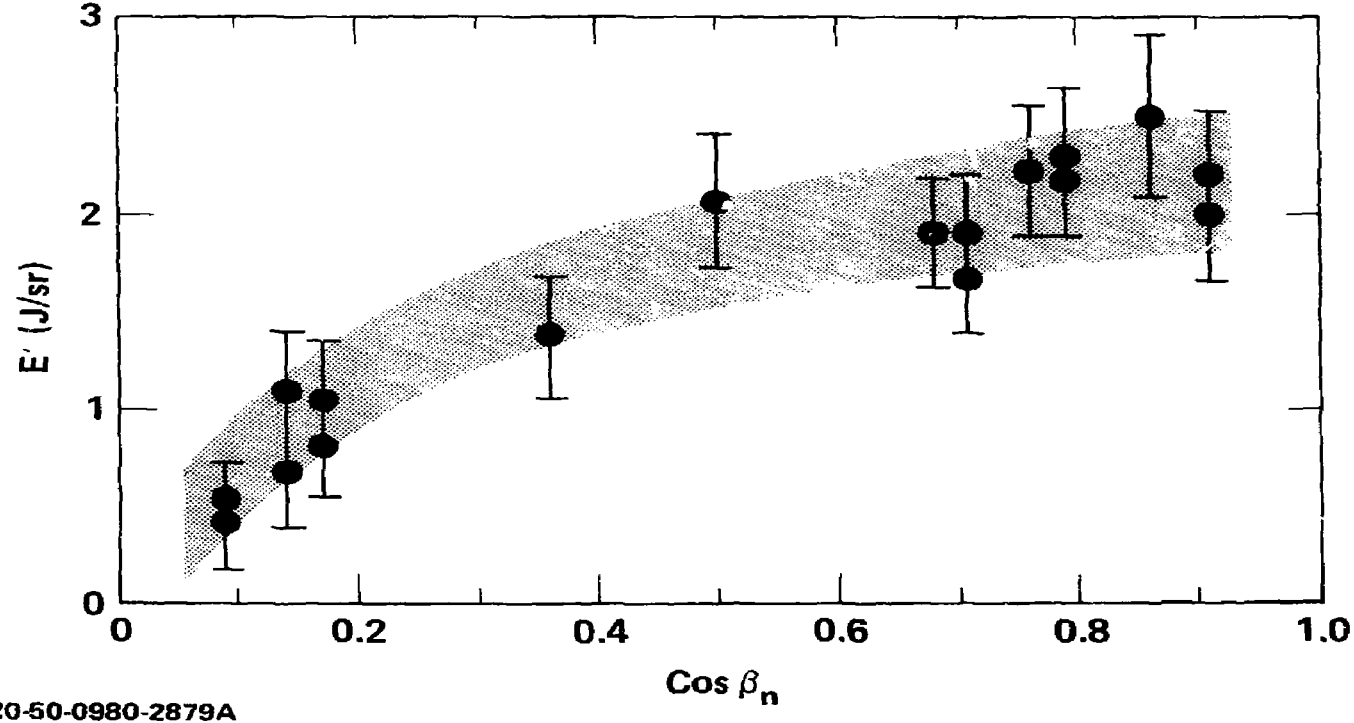

20-50-0980-2879A

Fig. 12 Angular distribution of x-ray emission from Au at I ~ 3 x 10^{14} W/cm^2 (25 Joules/600 psec.).

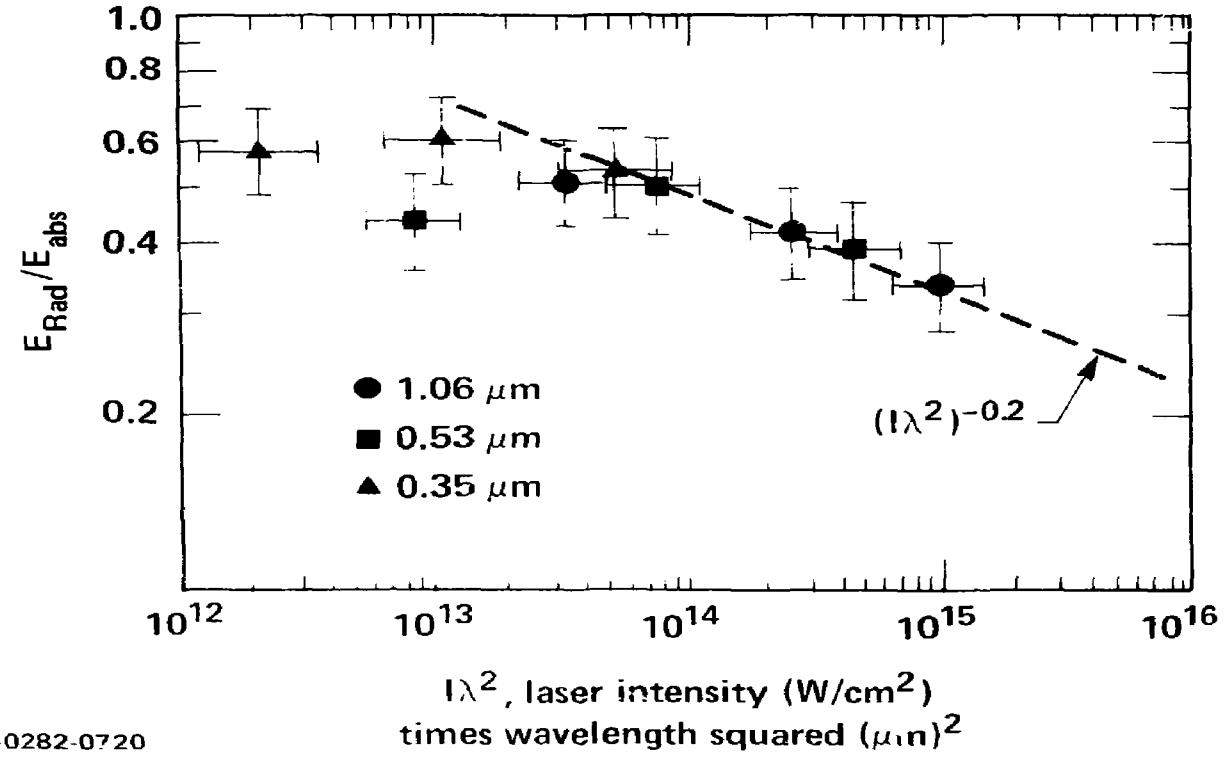

20-50-0282-0720

Fig. 13 Thermal x-ray conversion efficiencies from Au disk targets.

Figure 14 shows, the soft x-ray conversion efficiency appears to increase almost linearly with $\bar{Z}^{2.6}$

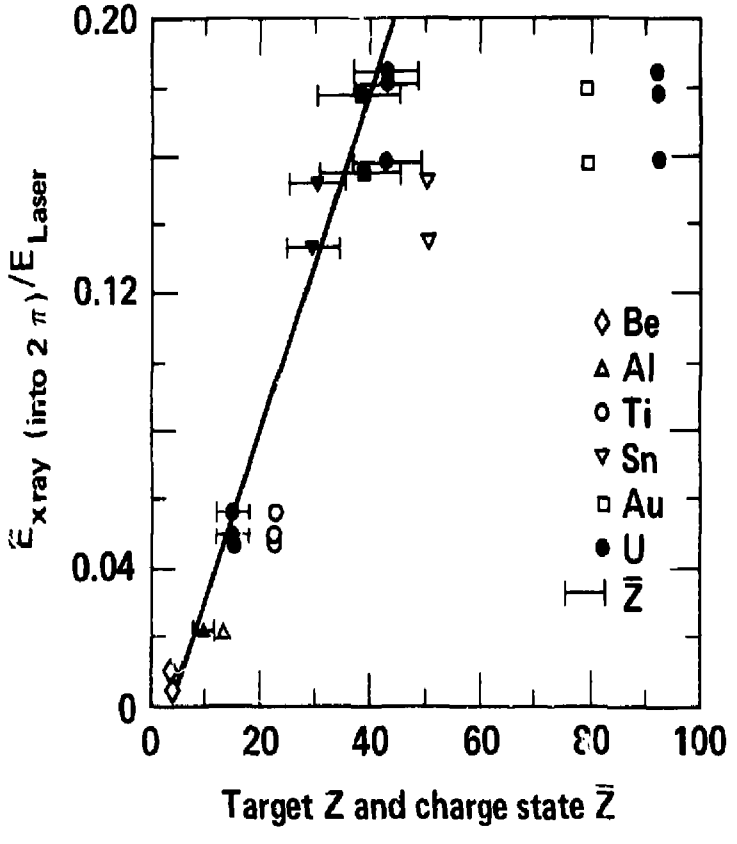

Fig. 14 X-ray energy for various targets as a function of target Z and charge state $\bar{Z}$, at incident intensity of 5 x 10^{14} W/cm^2. Error bars for values of $E_{x\text{-}ray}/E_{laser}$ are all ~ ± 25%.

X-RAY LINE PRODUCTION

High resolution crystal spectroscopy has revealed very complex line structures radiating from non-LTE laser heated targets.[25] This review can not even brush the surface of this fascinating field and must be restricted to a small part of the data accumulated during the past year. Fundamental to this sort of study is an absolute measurement of the amount of laser energy required to produce a given amount of "line" emission. The laser intensity, pulse duration and wavelength play a significant role. Qualitatively, long low intensity short wavelength laser pulses create enough hot plasma to allow copious production of

highly ionized atoms, which radiate He- and Li-like lines. Short high intensity long wavelength laser pulses produce suprathermal electrons which induce fluorescence lines in cold matter; these lines can dominate the radiated x-ray spectrum.

Motivated by a search for x-ray backlighter sources suitable for radiography of ICF targets, Rupert, Matthews and Koppel conducted a survey of lines in laser heated plasmas; concentrating on the K lines of Ti, Ni and Zn.[4] They defined a conversion efficiency, ξx, for an x-ray line emitter as the number of photons per line or line cluster divided by the incident laser energy. For all materials and laser irradiation conditions tested, $\xi x \cong 10^{11}$ to 10^{12} photons/J. The maximum measured conversion efficiencies are summarized in Figure 15.[4]

Figure 16, drawn from Ref. 4 and 17, shows the variation in spectral emission with laser wavelength. At the shorter wavelengths, all emissions are "thermal" (He- and Li-like); the spectra show no detectable level of the cold K_α line that is seen at $\lambda = 1.06\ \mu m$ and dominates the spectrum at $\lambda = 10.6\ \mu m$. Variations in ξx with incident laser intensity are illustrated by titanium data in Figure 17.[4] Below a fairly sharp threshold which depends on laser wavelength and pulse duration, x-ray lines were not observed. Above this threshold, the conversion efficiency increased with decreasing laser intensity as was the case with soft x-ray conversion efficiency. Although somewhat higher conversion efficiencies were observed for shorter wavelengths, at a given laser intensity there were no significant differences in ξx seen when the laser pulse duration was varied from 100 ps to 2 ns.

Much effort has gone into measuring the temporal and spatial extent of the x-ray emission from laser heated plasmas.[4,17,18,19] Typically, the x-ray flashes were the same or longer in duration than the laser pulses with K_α emission slightly (50 to 100 ps) delayed as though the suprathermal electrons exciting these lines were produced late, traveled outwards and reflected from coronal potentials before interacting with the cold matter. Spatially, He- and Li-like line emission was confined to the most vigorously heated region of the target while K_α emission was reported from somewhat larger areas.

SUPRATHERMAL ELECTRON MEASUREMENTS

Discrepancies between simulation and experimental observations have often been traceable to a poor understanding of high temperature coronal plasma physics. Not surprisingly, LASNEX simulations of the higher energy or suprathermal x-ray spectra observed are often in disagreement with the data.[4] Deviations are most pronounced in the five to fifteen keV range with good agreement below and, with a flux limiter parameter adjusted to fit, reasonable agreement at energies above about forty keV. LASNEX typically over estimates this mid-range x-ray flux from high Z targets.[4]

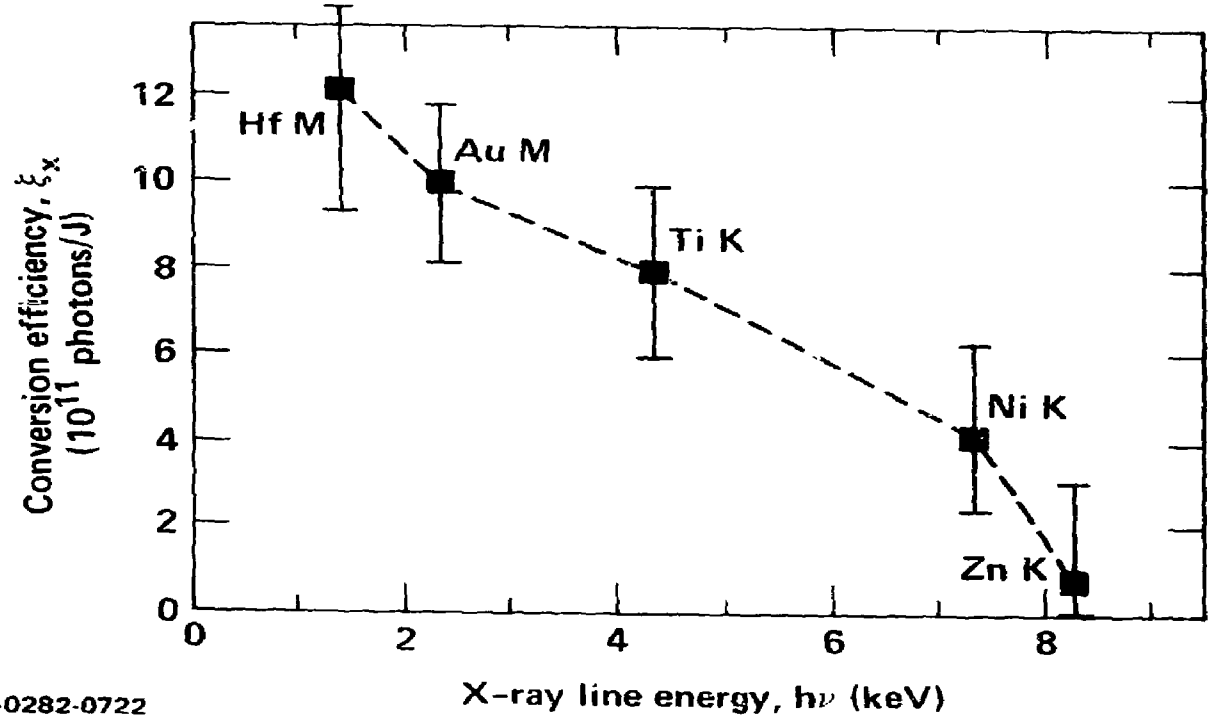

Fig. 15 Maximum measured conversion efficiencies for various backlighters.

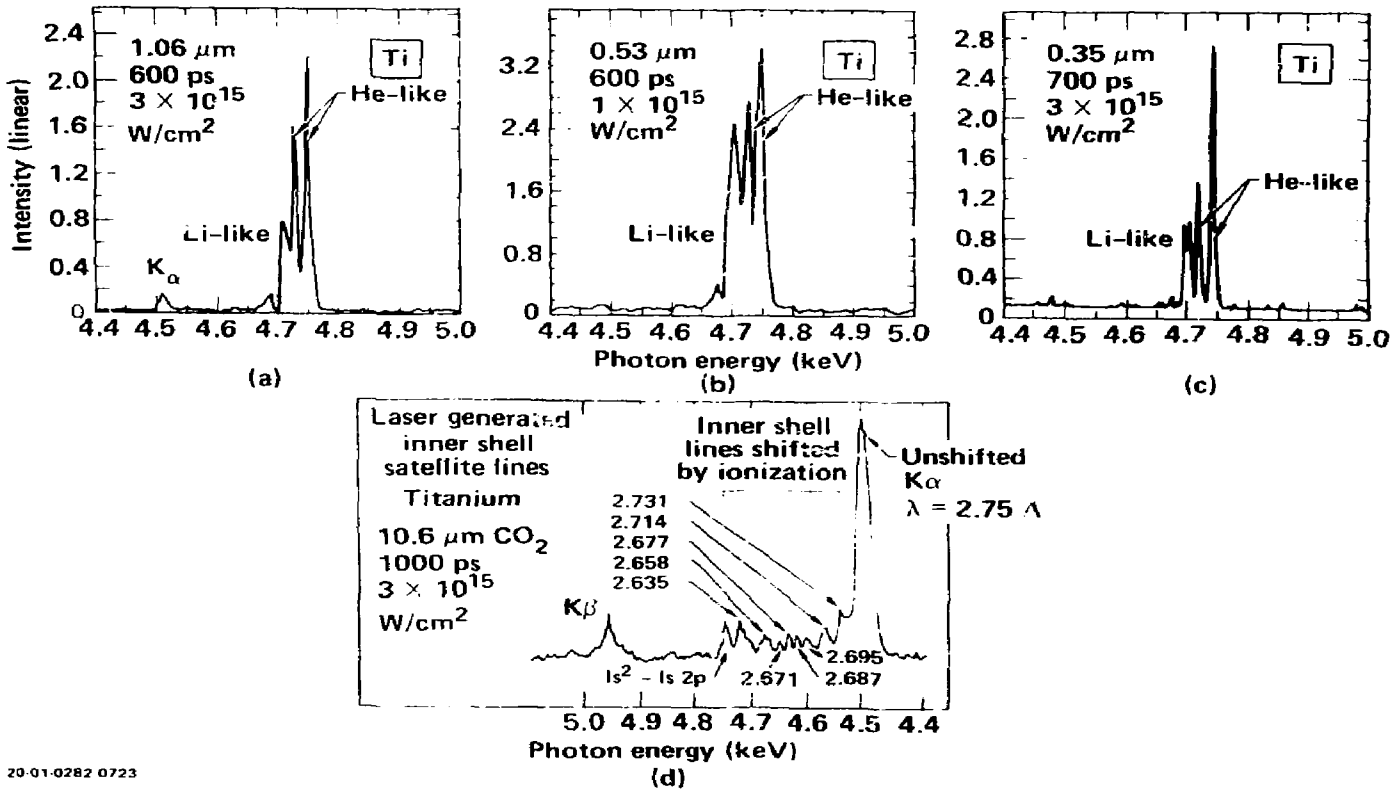

Fig. 16 Ti spectra for different laser wavelengths. Plots a), b) and c) are taken from Reference 4 while d) comes from Reference 17.

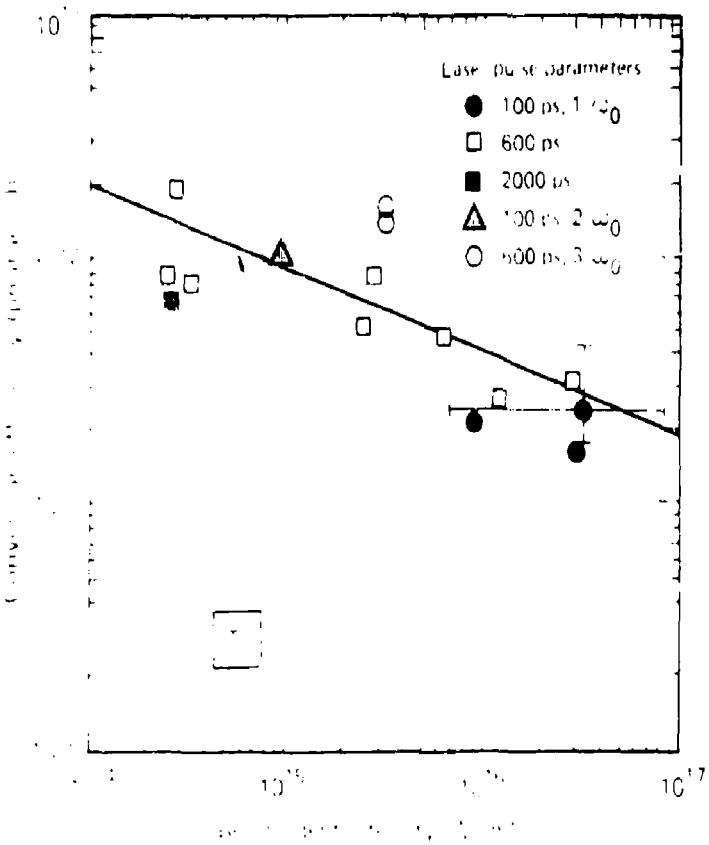

Fig. 17 Line-conversion efficiency as a function of laser intensity for Ti.

Two instrument packages provide the bulk of the LLNL suprathermal x-ray spectral information. A sensitive K-edge filtered four channel photomultiplier system was needed to record the weak suprathermal emission from 0.35 μm heated targets.[5,25] Higher intensity 1.06 μm irradiations produced sufficient flux to measure with a more accurate filter-fluorescer spectrometer.[5,25] Working together, these two spectrometers produced the spectra in Figure 18. By fixing intensity on target of approximately 3 x 10^{14} W/cm^2, the suprathermal spectra from Au plasmas can be compared as the laser wavelength is varied. The general trend is clear, shorter wavelength irradiations give rise to significantly fewer, cooler suprathermal electrons. The bremsstrahlung x-rays produced by suprathermal electron scattering from target ions provide a measure of the suprathermal electron population. While the data shown in Figure 18 for each wavelength and Au plasmas scatters over

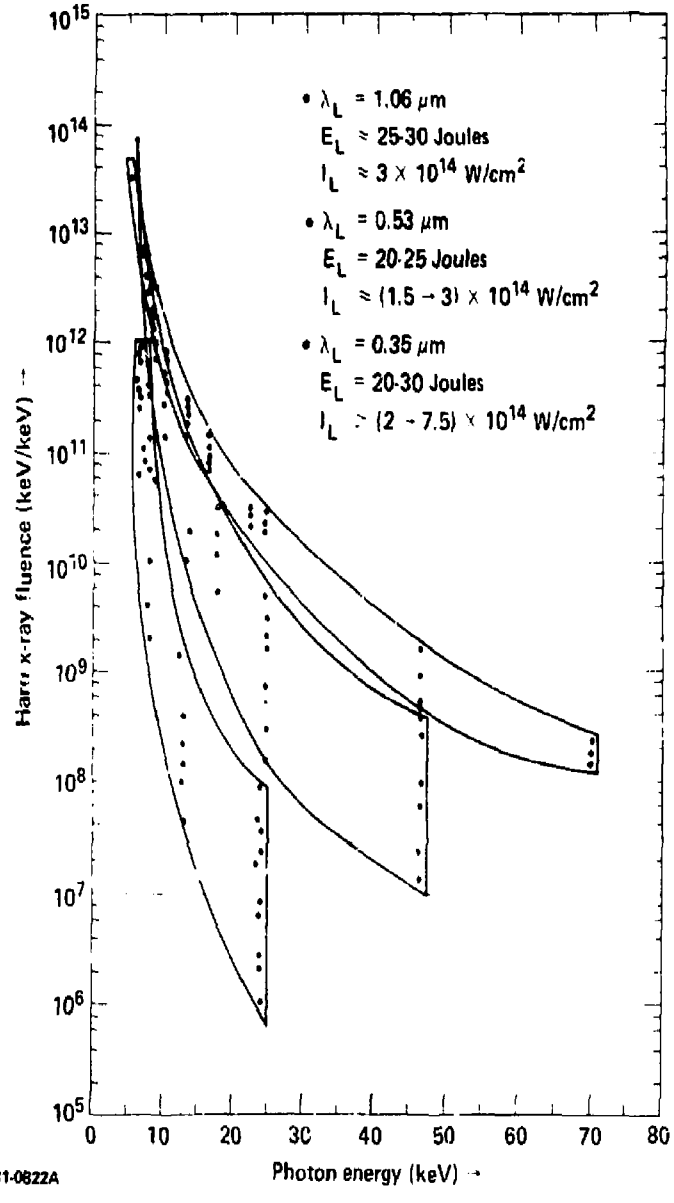

Fig. 18 The fraction of energy in hot electrons decreases drastically at shorter laser wavelengths.

as much as two decades, the measurements at each x-ray energy do not overlap. That is, the highest x-ray flux observed in 0.35 μm target irradiations lies below the lowest x-ray flux detected in 0.53 μm experiments employing the same average intensity on target. Simulation calculations typically do not employ the highly structured beam profiles with which these targets were irradiated. This, more than any other factor, contributes to the calculational uncertainty, experimental data scatter and concomitant disagreement between simulations and experiments.[4,20]

Like the soft x-ray conversion efficiency determinations, suprathermal x-ray flux measurements are sensitive to incident laser intensity. Figure 19 bins the data according to intensity and reveals that

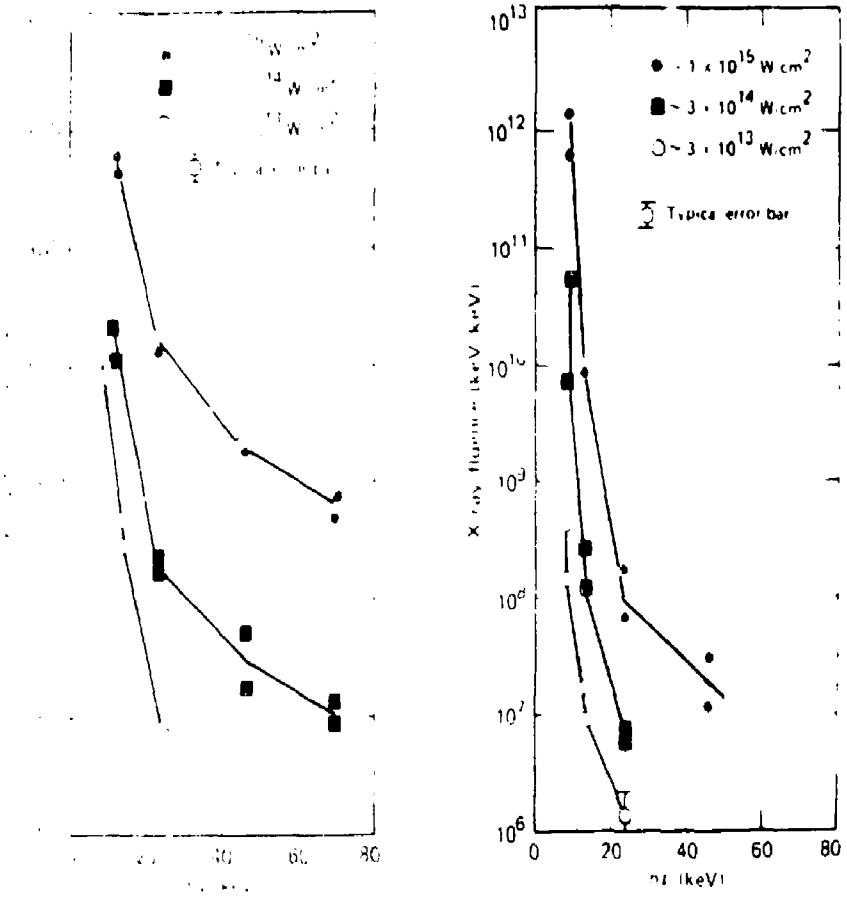

Fig. 19 Dependence of 2ω and 3ω x-ray fluence on laser-beam intensity.

suprathermal flux increases with increasing intensity on target. Once again, the scatter in the data is large probably due to beam quality, but the general trend is clear. Suprathermal x-ray spectra from plasmas whose heating is not dominated by resonance absorption, often do not exhibit the clear two temperature character evident in earlier short pulse 1.06 μm studies.[33] Assignment of unique intensity or wavelength dependent temperatures is not meaningful for spectra such as those in Figure 19.

Experimentally, there are two avenues to pursue. On the one hand, every reasonable effort must be expended to produce and reliably diagnose more uniform laser beams at the target. At the same time, the signatures of low density, high temperature coronal processes which might produce suprathermal electrons must be searched for in target emissions. Limited by time and optics availability, the disk experiments reported here did not involve attempts to significantly improve the laser beam profile. Optical spectrographs and filtered detectors were available, however, so scattering measurements were made at frequencies both above and below the target irradiation frequency to look at processes occurring at densities below $N_c/4$, i.e. Raman light and $3/2\omega_0$ light.[4] If resonant stimulated Raman scattering takes place in the coronal plasma, detectable quantities of light at twice the incident wavelength should be emitted out of the plane of polarization of the incident laser light. Refraction will cause this light to be observed near the target's normal. Non-resonant Raman scattering can occur at electron densities below $N_c/4$ and involves the decay of the incident photons at ω into electron plasma wave phonons at ω_{pe} and scattered photons at ω_s where energy conservation requires

$$\omega = \omega_s + \omega_{pe}$$

A related process, $2\omega_{pe}$ decay, might also be present. In this case, incident optical photons give up their energy to two electron plasma waves, both at ω_{pe}, and this can only be important near $N_c/4$. This latter process, like the Raman process, can give rise to very high phase velocity electron plasma waves whose wavelengths and energies are typical of suprathermal electron temperatures observed experimentally.[4,26] It is difficult to quantify the level of either of these processes because Raman scattered photons are often very close to their critical densities and hence may be absorbed while $2\omega_{pe}$ decay produces no scattered photons. Evidence for $2\omega_{pe}$ decay can come from electron emission measurements and optical spectroscopy at sum frequencies such as $3/2\omega$.

Time integrated and spectrally integrated Raman emission at 1ω and 2ω are shown in Figure 20.[4] Spectra of $3/2\omega$ emissions are displayed in Figure 21. The strongest Raman emission was observed out of the plane of the incident laser's polarization, as expected.[4] Angular and spectral integrals for Raman emissions from 1.06 μm heated disk targets are plotted against average incident intensity in Figure 22.[4] Like suprathermal x-ray emission, Raman and $3/2\omega$ light levels fall rapidly with reduced intensity on target, reduced plasma size, and shortened wavelength. In some cases, clear evidence of non-resonant Raman

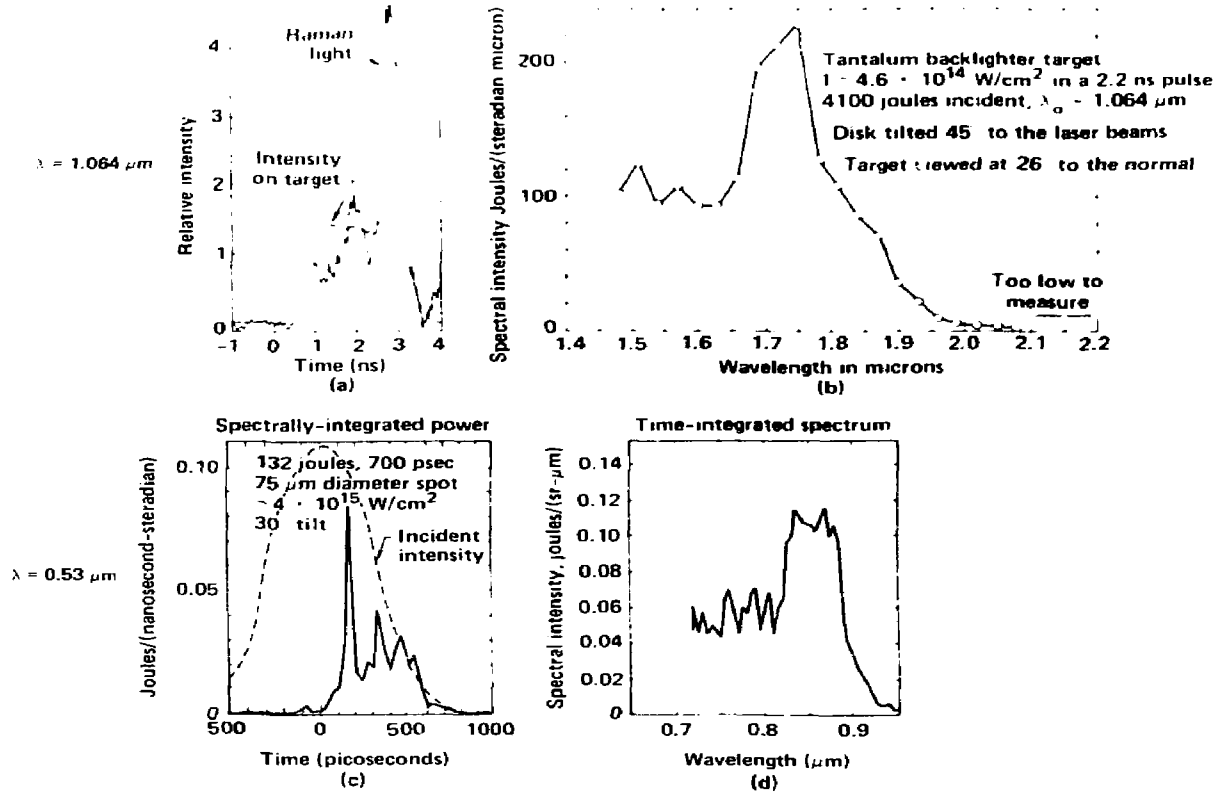

Fig. 20 Raman emission from laser heated high Z disk targets.

(a) Stimulated Raman spectrally-integrated power and (b) Raman light spectrum for a tantalum disk irradiated with 4100 J in a 2.2 ns pulse at 4.6 x 10^{14} W/cm^2.

(c) Time-resolved Raman light spectrum for a gold disk irradiated with 5320 Å light. Spectrally-integrated power and (d) Time-integrated spectrum.

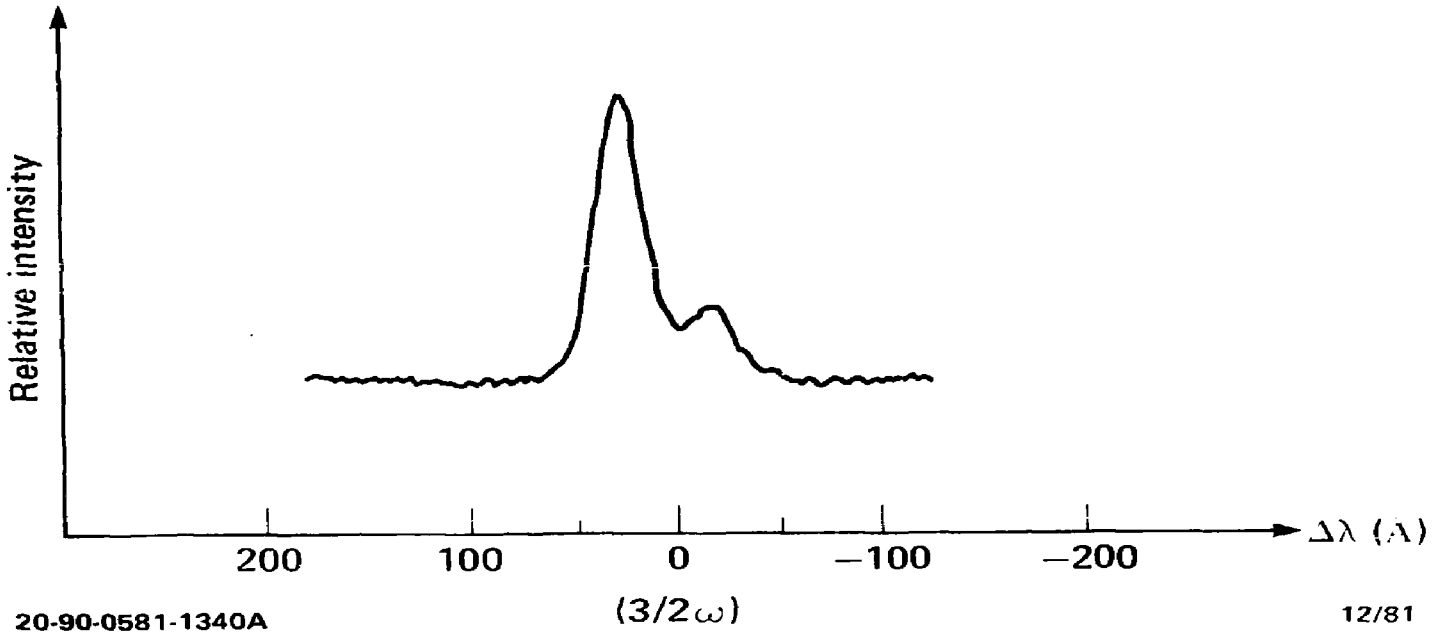

Fig. 21 Time integrated 3/2ω spectrum for an incident intensity of $I = 3 \times 10^{13} W/cm^2$, a Be disk target and laser wavelength = 1.06 μm. We observe a red peak shifted ~ 30Å and a blue peak shifted ≈ 20Å.

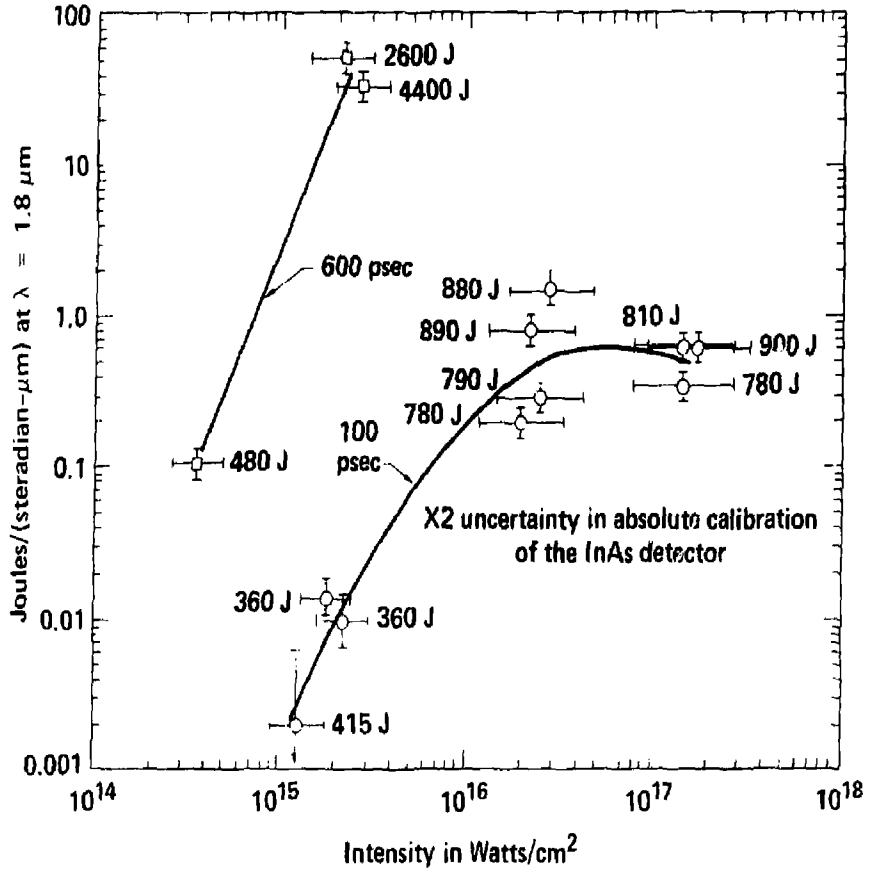

Fig. 22 Stimulated Raman scattering depends on the laser wavelength, the intensity and the size of the underdense plasma.

sidescattering has been obtained. Figure 23, reproduced from Reference 4, shows wavebreaking energies expected for stimulated Raman scattering in 5 keV electron plasma temperatures. For example, the Raman spectrum displayed in Figure 20b indicates that substantial amounts of Raman energy was sidescattered at electron densities near $0.1N_c$. Raman backscatter may be excluded because at $N/N_c \simeq .05$, $K\lambda_D$ and thus Landau damping would be too large. Figure 24 is the suprathermal x-ray spectrum measured on that same shot. The slope of this spectrum suggests a suprathermal temperature of ~40 keV in good agreement with the Raman sidescatter wavebreaking energy for $0.1N_c$ shown in Figure 23. Data is therefore in hand which ties unique suprathermal electron temperatures to Raman scattered spectra. Where they exist, data such as that in Figure 20 together with the model used to calculate Figure 23 can be used as a plasma electron temperature diagnostic.[4] The Raman spectrum can

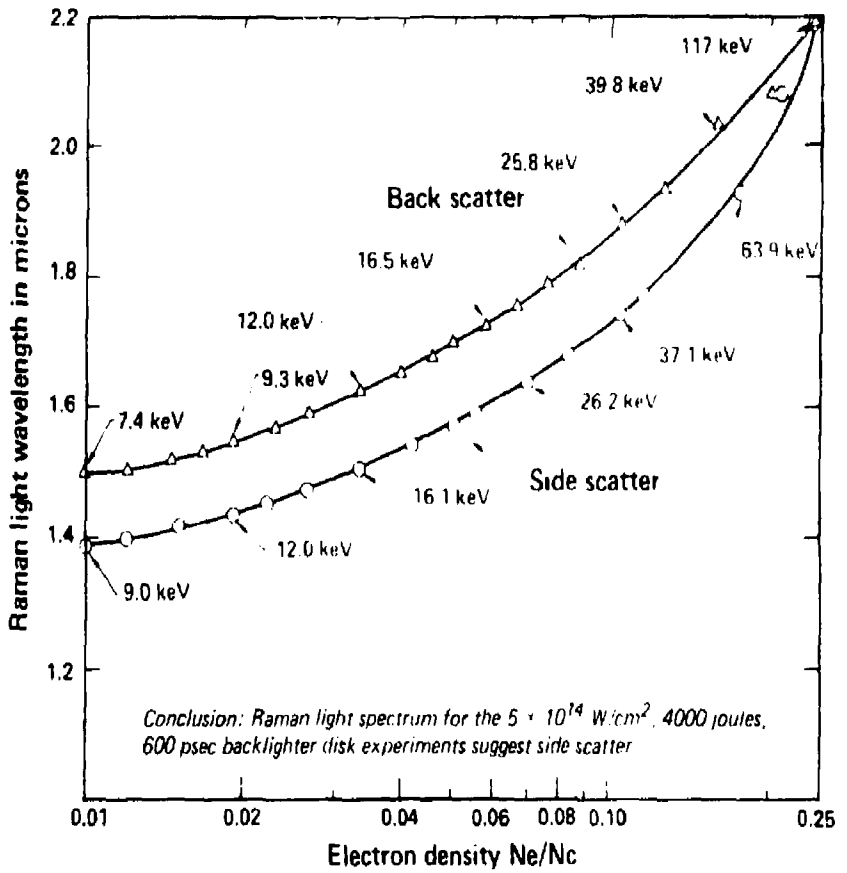

Fig. 23 Comparison of the solutions to the dispersion equations for side and backscatter at 5 keV.

provide an estimate of low density coronal electron temperature since the shifts are large compared to the Doppler shifts. As noted with stimulated Brillouin scattering, lowered coronal temperatures can be obtained at lowered intensities or shortened incident laser wavelength. Although Raman light levels from disk target studies are energetically small, the Raman light and $3/2\omega_0$ levels rise rapidly as the irradiating pulse duration and hence the volume of scattering plasma is increased. Figures 20a and c show time resolved Raman signals which clearly grow with time into the laser pulse. Raman and $2\omega_{pe}$ instabilities must therefore be carefully controlled lest they become important mechanisms for suprathermal electron production. These studies suggest that these instabilities can be suppressed simply by employing short wavelength lasers to drive ICF targets.

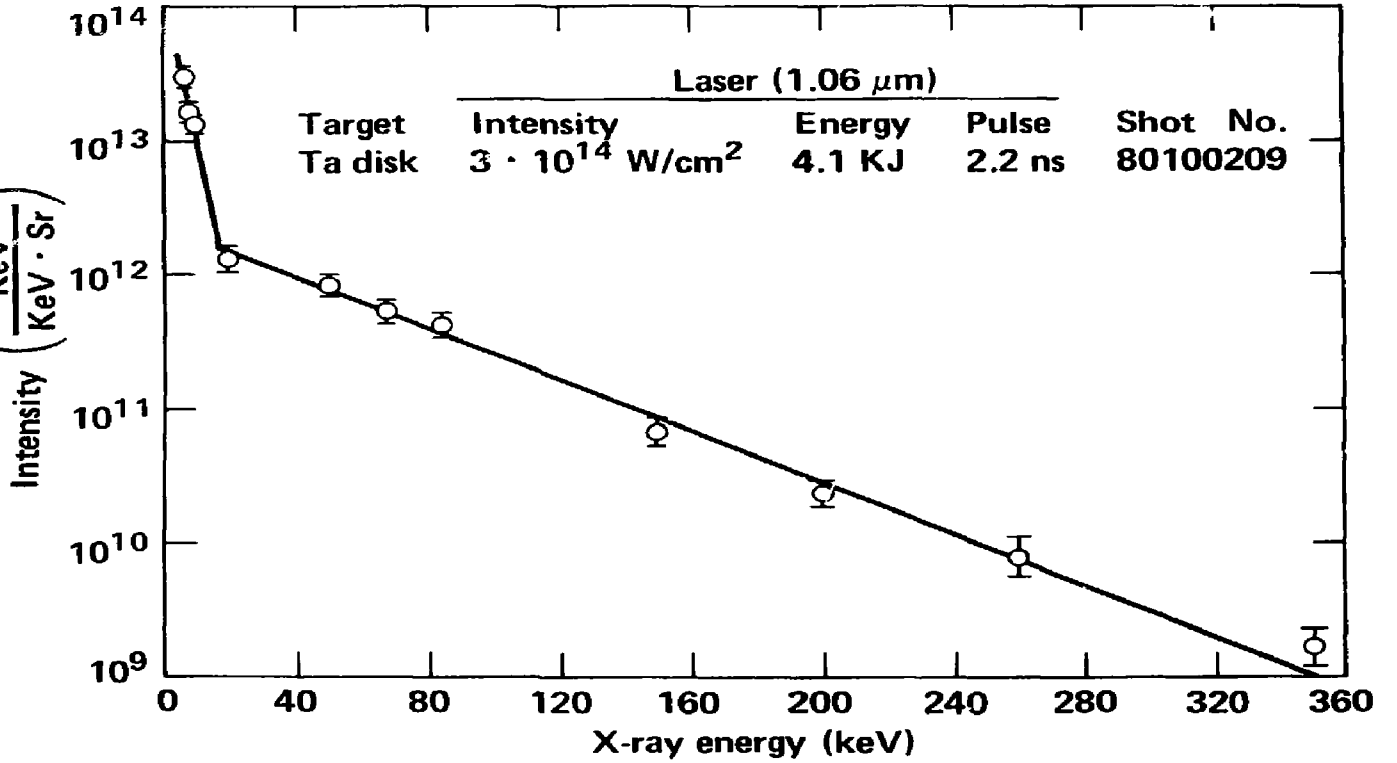

Fig. 24 Suprathermal x-ray spectrum.

ENERGY PARTITION

The proceeding sections provide a basis for determining the relative fractions of the incident laser energy which is absorbed and then partitioned into soft x-ray emissions, thermal and suprathermal electron populations. Table III summarizes these findings for Au plasmas irradiated at each wavelength at an average incident intensity of $3 \times 10^{14} W/cm^2$. Substantially cooler coronal plasmas, free of severe electron plasma wave instabilities which simultaneously radiate efficiently in the soft x-ray spectral region can be realized by shortening the irradiating laser wavelength.

Taken together, stimulated scattering spectra and time-resolved x-ray images provide average fluid velocity estimates at several electron densities. Figure 25 indicates the observed relationships for Au disk targets in the range of peak average powers explored.[4]

The data in hand is sparse and the scalings suggested in Figure 13 and 25 may not survive future studies. It is remarkable, however, how well the simple scaling arguments put forward by Rosen et al describe the plasma behavior.[4,12] The model assumes that electron thermal conduction transports energy from the laser absorption region (at critical density, $N_e = N_c \simeq (10^{21}/\lambda^2)$ electrons/cm^3 for λ in μm) to the overdense plasma. Equating absorbed laser flux, I_a, with the heat flux carried off by the plasma, $N_c T_e v_e$, leads to the relation $I_a \lambda^2 \sim T_e^{3/2}$.[12] To use this expression, the model assumes that the plasma is expanding outward (toward the laser) at the local ion sound speed which scales as the square root of pressure divided by density, $v \sim C_s \simeq (P/\rho)^{1/2} \sim (\bar{Z}T)^{1/2}$ and that T is proportional to T_e. Table II shows that near Nc/3, $\bar{Z}$ varies weakly with Te for $Te > 2$ keV. Neglecting this $\bar{Z}$ dependence leads to

$$v \sim \left(I_a \lambda^2\right)^{1/3} \tag{3}$$

which may be compared to the velocities inferred from SBS spectra in Figure 25.

Since dense material radiates more efficiently than less dense material at a given temperature, the soft x-ray emission peaks at the highest density reached by the thermal-conduction front.[4] For example, bremsstrahlung from a single species hydrogen-like plasma may be written

$$P_{Br} \simeq 1.6 \times 10^{-34} \left(T_e^{1/2} \bar{Z}^3 N_i^2\right) \text{ Watts/cm}^3 \tag{4}$$

where N_i is the ion density.[21]

Rosen assumes that the temperature, which is falling rapidly near the thermal front as it propagates into the dense plasma, is proportional the temperature, T_e, in the absorption region. Equations of state for gold indicate that, for T less than 1 keV, $\bar{Z} \approx 1.6 \left[T(ev)\right]^{1/2}$ so the sound

TABLE III

Absorbed Energy Partition at $I \sim 3 \times 10^{14} W/cm^2$

Au Disk Targets

	1.06 μm	0.53 μm	0.35 μm
Soft x-ray flux	0.4 ± 0.1	0.5 ± 0.1	0.6 ± 0.1
Coronal hydro	0.6 ± 0.1	0.5 ± 0.1	0.4 ± 0.1
Suprathermal electrons	0.03 to 0.06	0.01 to 0.001	0.001 to 0.0001

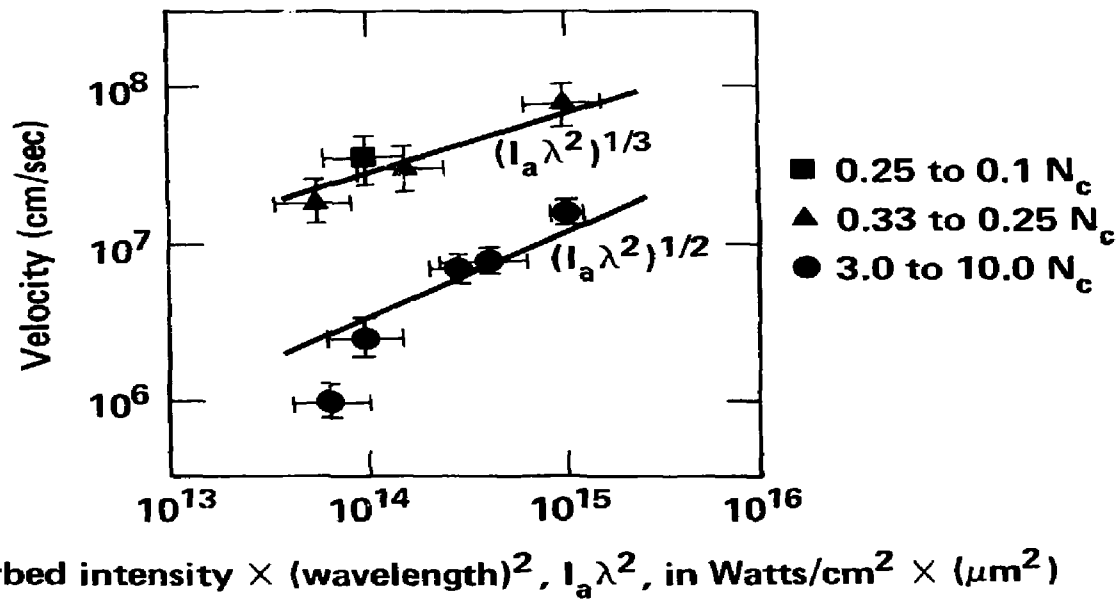

Fig. 25 Fluid flow velocities estimated from stimulated scattering and time resolved x-ray images. One dimensional current continuity would require $N_e v_e \cong$ constant and one dimensional mass continuity would require $N_i v \cong$ constant so it was not surprising that typical velocities in the subcritical plasma are about ten times higher than those in the denser x-ray emission region. The solid lines come from the scaling arguments of Rosen et al.[4,12]

speed in the peak soft x-ray emission region should scale as $T^{3/4}$ or

$$(I_a \lambda^2)^{1/2.4} \tag{5}$$

By assuming that inverse bremsstrahlung is the dominant absorption mechanism, Rosen arrives at a scaling for the temperature in the absorption region in terms of the incident laser intensity, $T \sim I^{0.6}$.[12] Thus, the peak velocity of the emission region should scale as $v \sim I^{0.45}$ which is within the experimental error range, $v \sim I^{0.44 \binom{+0.22}{-0.17}}$.[4]

The same model crudely estimates that for fixed laser pulse duration the depth of penetration of the thermal conduction front is proportional to temperature, T_e.[4] Time resolved x-ray images such as that in Figure 9 showed the width of the emission region to scale as $I^{0.7 \pm 0.25}$ in keeping with this model.

Soft x-ray spectra such as those in Figure 10 show the non-local-thermodynamic equilibrium of these disk plasmas. Strong Au N-band emission near 800 ev is apparent, particularly at the higher incident intensities, and the spectra are hardly Plankian. It is interesting, nevertheless, to apply the same model to single species bremsstrahlung emission. Emitted intensity would vary as

$$I_{Br} \sim \bar{Z}^3 N_i^2 T_e^{3/2}. \tag{6}$$

Given current continuity; i.e. that $N_e v_e = Z N_i T_e^{1/2}$ is nearly constant into the material for each absorption region temperature, the emitted intensity can be written

$$I_{Br} \sim \bar{Z} T_e^{1/2} \sim T \sim I_a^{2/3}. \tag{7}$$

Consequently this part of the x-ray conversion efficiency would scale as

$$\eta_{Br} = I_{Br}/I_a \sim I_a^{-1/3} \tag{8}$$

Which suggests that the x-ray conversion efficiency should decline weakly as I_a increases. Similarly, given mass continuity, i.e. $N_i v \sim N_i \bar{Z}^{1/2} T^{1/2}$ is nearly constant into the material, the emitted intensity becomes

$$I_{Br} \sim \bar{Z}^2 T_e^{1/2} \sim T^{3/2} \sim I_a. \tag{9}$$

This scaling suggests that the x-ray conversion efficiency is roughly independent of I_a. Figure 13 shows the total x-ray conversion efficiency scaling as $(I\lambda^2)^{-0.2}$ for $I\lambda^2 > 10^{13}$. Without accurate x-ray line production and transport calculations, however, quantitative modeling of x-ray production is impossible.

Simulation of sub-critical density plasma is an even greater challenge. Fortunately, the data available to us suggests that suprathermal electron production may be made energetically unimportant by short wavelength irradiation. ICF target designers can thus avoid most of their preheat problems by specifying short laser wavelength.[24]

ACKNOWLEDGEMENTS

The experiments reviewed here were carried out by the members of the Experiments Group, an element of H. G. Ahlstrom's Fusion Experiments Program, while the author had the privilege of leading that group. Senior members of the Experiments group during this interval included J. Auerbach, D. Banner, E. Campbell, D. Matthews, D. Phillion, V. Rupert, R. Turner, and F. Ze. Experiments of this scope would have been impossible without the enthusiastic support of the Target Fabrication Program under C. Hendricks, the Diagnostics Group under W. Slivinsky and the Laser Systems Operations Group under D. Barr and J. Hunt. Finally, the design and analysis of these studies was carried out in close collaboration with John Nuckolls' target design program whose simulation calculations are our best guide in the search for practical inertial confinement fusion.

REFERENCES

1. E. Fabre et al, in Proceedings of the Conference on Plasma Physics and Controlled Nuclear Fusion Research, Vienna, Austria, 1980 (International Atomic Energy Agency, Vienna, 1981), Paper No. IAEA-CN-38/1-4.

2. A. G. M. Maaswinkel, K. Eidmann, and R. Sigel, Phys. Rev. Lett. 42, 1625 (1979); O. E. Slater et al, Phys. Rev. Lett. 46, 1199 (1981); W. Seka et al, Bull. Am. Phys. Soc. 25, 895 (1980).

3. M. C. Mead, E. M. Campbell, R. E. Turner, W. L. Kruer, P. H. Y. Lee, B. Pruett, V. C. Rupert, K. G. Tirsell, G. L. Stradling, F. Ze, C. E. Max, and M. D. Rosen, "Laser-Plasma Interactions at 0.53 μm for Disk Targets of Varying Z", Phys. Rev. Lett. 46, 1289 (1981).

4. Section 7 of "Laser Program Annual Report - 1980", Lawrence Livermore National Laboratory, Livermore, California, UCRL-50021-80, pages 7-? to 7-?6 (1981).

5. H. G. Ahlstrom, "Laser Fusion Experiments, Facilities and Diagnostics at Lawrence Livermore National Laboratory", Applied Optics 20, 1902 (1981).

6. J. Nuckolls et al, Nature (London) 239, 139 (1972).

7. J. H. Gardner and S. E. Bodner, "Wavelength Scaling for Reactor-Size Laser Fusion Targets", NRL Memorandum Report 4623, Naval Research Laboratory, (1981).

8. C. E. Max, C. F. McKee, and W. C. Mead, Phys. Fluids 23, 1620 (1980).

9. C. E. Max and K. G. Estabrook, Comments Plasma Phys. Controlled Fusion 5, 239 (1980).

10. D. R. Speck et al, "The Performance of Argus as a Laser Fusion Facility", Lawrence Livermore National Laboratory, Livermore, California, UCRL-52487.

11. D. R. Speck et al, "The Shiva Laser-Fusion Facility", IEEE Journal of Quantum Electronics QE-17, 1599 (1981).

12. M. D. Rosen et al, Phys. Fluids 22, 2020 (1979).

13. K. Estabrook et al, Phys. Rev. Lett. 46, 724 (1981).

14. M. Herbst et al, NRL Memorandum #4436 and BAPS 26, 1024 (1981).

15. Section 5 of "Laser Program Annual Report - 1980", Lawrence Livermore National Laboratory, Livermore, California, UCRL-50021-80, pages 5-23 to 5-31.

16. C. F. Max et al, BAPS 26, 873 (1981).

17. A. Hauer et al, Applied Optics 20, 3077 (1981).

18. V. Rupert, D. L. Matthews and L. N. Koppel, "X-ray Backlighting Sources of 4 to 10 keV for Laser Fusion Targets", presented at the 1st European Conference on Cineradiography with Photons or Particles, UIC, Paris, France, May 1981, UCRL-85592 (1981).

19. J. D. Hares, J. D. Kilkenny, M. H. Key and J. G. Lunney, Phys. Rev. Lett. 42, 1216 (1979).

20. B. Arad and S. Eliezer, Appl. Phys. Lett. 32, 401 (1978).

21. D. L. Book, "NRL Plasma Formulary", NRL Memorandum Report No. 2898.

22. K. R. Manes, V. C. Rupert, J. M Auerbach, P. Lee, and J. E. Swain, Phys. Rev. Lett. 39, 281 (1977).

23. K. R. Manes, H. G. Ahlstrom, R. A. Haas, and J. F. Holzrichter, J. Opt. Soc. Am., 67 717 (1977).

24. R. L. McCrory, BAPS 26, 972 (1981) and references cited therein.

25. Low Energy X-ray Diagnostics - 1981, Edited by D. T. Attwood and B. L. Henke, American Institute of Physics Conference Proceedings No. 75, New York, (1981).

26. Section 6 of "Laser Program Annual Report - 1979", Lawrence Livermore National Laboratory, Livermore, California, UCRL-50021-79 (1980).